

# Effect of Hydrostatic Pressure on Lone Pair Activity and Phonon Transport in $\text{Bi}_2\text{O}_2\text{S}$

Neelam Yedukondalu,<sup>\*,†,‡,¶</sup> Tribhuwan Pandey,<sup>\*,§</sup> and S Chand Rakesh Roshan<sup>||,⊥</sup>

<sup>†</sup>*Department of Analytical and Structural Chemistry, CSIR-Indian Institute of Chemical Technology, Tarnaka, Hyderabad 500007, India*

<sup>‡</sup>*Department of Geosciences, Center for Materials by Design, and Institute for Advanced Computational Science, State University of New York, Stony Brook, New York 11794-2100, USA*

<sup>¶</sup>*Joint Photon Sciences Institute, Stony Brook University, Stony Brook, New York 11790-2100, USA*

<sup>§</sup>*Department of Physics, University of Antwerp, Groenenborgerlaan 171, B-2020 Antwerp, Belgium*

<sup>||</sup>*Rajiv Gandhi University of Knowledge Technologies, Basar, Telangana-504107, India*

<sup>⊥</sup>*Department of Physics, National Institute of Technology-Warangal, Telangana, India*

E-mail: nykondalu@gmail.com; tribhuwan.pandey@uantwerpen.be

## Abstract

Dibismuth dioxychalcogenides,  $\text{Bi}_2\text{O}_2\text{Ch}$  (Ch = S, Se, Te) are emerging class of materials for next generation electronics and thermoelectrics with an ultrahigh carrier mobility and excellent air stability. Among these,  $\text{Bi}_2\text{O}_2\text{S}$  is fascinating because of stereochemically active  $6s^2$  lone pair of  $\text{Bi}^{3+}$  cation, heterogeneous bonding and high mass contrast of constituent elements. In this work, we systematically investigate the effect of hydrostatic pressure and its implications on lattice dynamics and phonon transport properties of  $\text{Bi}_2\text{O}_2\text{S}$  by employing first principles calculations along with the Boltzmann transport theory. The ambient  $Pn\bar{m}n$  phase exhibits a low average lattice thermal conductivity ( $\kappa_l$ ) of 1.71 W-m/K at 300 K. We also find that  $\text{Bi}_2\text{O}_2\text{S}$  undergoes a structural phase transition from low symmetry ( $Pn\bar{m}n$ ) to a high symmetry ( $I4/m\bar{m}m$ ) structure around 4 GPa due to the  $\text{Bi}^{3+}$  cation centering. Upon compression the lone pair activity of  $\text{Bi}^{3+}$  cation is suppressed, which increases  $\kappa_l$  by nearly 3 times to

4.92 W-m/K at 5 GPa for  $I4/m\bar{m}m$  phase. The calculated phonon lifetimes and Grüneisen parameters show that anharmonicity reduces with increasing pressure due to further suppression of lone pair, strengthening of intra and inter molecular interactions, which raises the average room temperature  $\kappa_l$  to 12.82 W-m/K at 20 GPa. Overall, the present study provides a comprehensive understanding of hydrostatic pressure effects on stereochemical activity of the  $\text{Bi}^{3+}$  cation lone pair and its consequences on phonon transport properties of  $\text{Bi}_2\text{O}_2\text{S}$ .

**Keywords:** Lone pair, Stereochemical activity, Lattice dynamics, Phonon transport, Hydrostatic pressure

## Introduction

Chemical intuitions are central for the development of cutting edge technologies to exploit the renewable energy resources for thermal energy management applications. For example, the lone pair electrons are important for re-

alizing low lattice thermal conductivity ( $\kappa_l$ ) by inducing strong anharmonicity in the system.<sup>1-5</sup> Similarly, layered structures promote strong bonding heterogeneity (combination of rigid and fluctuating sub-lattices in a material) and has important implications to enhance complex interdependent thermoelectric properties, such as high power factor and low  $\kappa_l$ .<sup>6,7</sup> Recently, dibismuth dioxchalcogenides,  $\text{Bi}_2\text{O}_2\text{Ch}$  (Ch = S, Se, Te), and their 2D counterparts<sup>8-12</sup> have gained tremendous research interest due to their potential applications in thermoelectrics,<sup>11,13,14</sup> ferroelectrics,<sup>15</sup> and optoelectronics.<sup>9,11,16-18</sup> Among these,  $\text{Bi}_2\text{O}_2\text{S}$  is unique due to stereochemically active  $6s^2$  lone pair of  $\text{Bi}^{3+}$  cation, and hence, it crystallizes in the primitive orthorhombic structure (SG:  $Pnmm$ , Z=2 formula units (f.u.) per primitive cell), while  $\text{Bi}_2\text{O}_2(\text{Se/Te})$  crystallizes in the body centred tetragonal (SG :  $I4/mmm$ , Z = 1 f.u. per primitive cell) anti- $\text{ThCr}_2\text{Si}_2$ -type structure. These crystals are made of alternating  $\text{Bi}_2\text{O}_2$ , and chalcogen (S/Se/Te) layers, which are held together by weak electrostatic forces<sup>19,20</sup> in contrast to van der Waals (vdW) interactions that are typically observed in layered materials.<sup>21-23</sup> Infra-red and Raman spectra<sup>24</sup> and strain effects on bulk and monolayer  $\text{Bi}_2\text{O}_2\text{Ch}$  crystals are systematically investigated to explore their possible applications in nano-electronics.<sup>25</sup>

A high pressure X-ray diffraction study<sup>26</sup> revealed that  $\text{Bi}_2\text{O}_2\text{S}$  undergoes a structural transition from  $Pnmm \rightarrow I4/mmm$  at 6.4 GPa due to displacive nature of off-centred  $\text{Bi}^{3+}$  cation and then 2D  $\rightarrow$  3D structure upon further compression above 13.2 GPa owing to disappearance of the  $6s^2$  lone pair.  $\text{Bi}_2\text{O}_2\text{Se}$  is one of the most stable Sillen-type compounds under pressure with no structural transition being observed until 30 GPa<sup>27</sup> while  $\text{Bi}_2\text{O}_2\text{Te}$  is found to be stable till 50 GPa.<sup>28</sup> The intrinsic ultralow  $\kappa_l$  behavior<sup>20,29-31</sup> and thermoelectric properties<sup>29,31</sup> of  $\text{Bi}_2\text{O}_2\text{Ch}$  are studied using first principles calculations and Boltzmann transport theory. Effect of hydrostatic pressure on stereochemically active lone pair and its implications on lattice dynamics and phonon transport of  $\text{Bi}_2\text{O}_2\text{S}$  are scarce in the literature.

Here, we systematically investigate the crystal and electronic structure, elastic properties, lattice dynamics, and phonon transport properties for the ambient ( $Pnmm$ ) and high pressure ( $I4/mmm$ ) phases of  $\text{Bi}_2\text{O}_2\text{S}$ . By analyzing pressure-dependent static enthalpy, lattice, bond parameters, and elastic constants, we show that  $\text{Bi}_2\text{O}_2\text{S}$  undergoes a structural phase transition from low symmetry ( $Pnmm$ ) to a high symmetry ( $I4/mmm$ ) structure around 4 GPa. By analysis of electron localization function (ELF) and electronic structure, we further show that under pressure the lone pair electrons of  $\text{Bi}^{3+}$  cation are suppressed. This suppression of lone pair electrons reduces anharmonicity at high pressure and hence  $\kappa_l$  is enhanced.

## Computational details and Methodology

### Structure relaxation and electronic structure

The first calculations have been performed using Vienna Ab-initio Simulation Package (VASP).<sup>34</sup> The electron-electron interactions *i.e.* exchange-correlation are treated by Generalized Gradient Approximation (GGA) within the parametrization of Perdew-Burke-Ernzerhof (PBE). The electron-ion interactions are treated with pseudopotential approach. We have used DFT-D3 method<sup>35</sup> to capture the weak electrostatic interactions. The following plane wave basis orbitals were considered as valence electrons; Bi:  $5d^{10}, 6s^2, 6p^3$ ; O:  $2s^2, 2p^4$ ; and S:  $3s^2, 3p^4$ . A kinetic energy cutoff of 600 eV was used for plane wave basis set expansion and a spacing of  $2\pi \times 0.025 \text{ \AA}^{-1}$  for k-mesh in the irreducible Brillouin zone. The plane wave cutoff energy as well as k-spacing were varied first to ensure the total energy convergence. Self consistency criteria is chosen in such way that the total energy is converged to  $1e^{-8}$  eV/atom and the maximal force on each atom is less than  $1e^{-3}$  eV/ $\text{\AA}$ . Electronic structure is calculated using Tran Blaha modified Becke Johnson (TB-mBJ) potential<sup>36</sup> as implemented in VASP including spin-orbit coupling. Crystal

Table 1: Ground state structural properties such as lattice constants (a, b, c, in Å) and volume (V in Å<sup>3</sup>) of ambient (*Pnmn*) and high pressure (*I4/mmm*) phases of Bi<sub>2</sub>O<sub>2</sub>S obtained using DFT-D3 method and compared with the X-ray diffraction measurements.<sup>26</sup>

Phase	Parameter	This work	Expt. <sup>a</sup>	Others
<i>Pnmn</i> (0 GPa)	a	3.931	3.874	3.85 <sup>b</sup> , 3.9 <sup>c</sup> , 3.89 <sup>d</sup> , 3.837 <sup>e</sup> , 3.972 <sup>f</sup>
	b	3.861	3.840	3.89 <sup>b</sup> , 3.87 <sup>c</sup> , 3.87 <sup>d</sup> , 3.848 <sup>e</sup> , 3.884 <sup>f</sup>
	c	11.948	11.916	11.97 <sup>b</sup> , 12.05 <sup>c</sup> , 11.99 <sup>d</sup> , 11.94 <sup>e</sup> , 12.079 <sup>f</sup>
	V	181.34	177.264	-
<i>I4/mmm</i> (5.6 GPa)	a	3.787	3.7705	-
	c	11.713	11.6902	-
	V	167.97	166.211	-

<sup>a</sup>Ref.<sup>26</sup> <sup>b</sup>Ref.<sup>15</sup> <sup>c</sup>Ref.<sup>25</sup> <sup>d</sup>Ref.<sup>32</sup> <sup>e</sup>Ref.<sup>24</sup> <sup>f</sup>Ref.<sup>33</sup>

structures and electron localization functions are visualized using the VESTA software.<sup>37</sup> Local Orbital Basis Suite Towards Electronic Structure Reconstruction (LOBSTER) package<sup>38</sup> is used to perform crystal orbital Hamiltonian population (COHP) analysis.

## Interatomic force constants

Harmonic and anharmonic interatomic force constants (IFCs) are needed to calculate phonon thermal conductivity  $\kappa_l$  from first principles calculations. For both the phases, harmonic IFCs were obtained using the finite displacement method within the Phonopy package<sup>39</sup> with  $5 \times 5 \times 2$  (500 atoms) supercell and  $\Gamma$ -point only k-grid. Other parameters are same as those used in the structural relaxation. Long range corrections to phonon frequencies were included by calculation of Born effective charges and dielectric constants within the method proposed by Wang et. al.<sup>40</sup> Anharmonic IFCs were calculated using  $4 \times 4 \times 2$  supercell. For the displaced supercells configurations phonon-phonon interactions were considered up to the 5.5 Å distance. This requires 900 and 500 DFT calculations for *Pnmn* and *I4/mmm* phases, respectively. The rest of the parameters are same as those used in the harmonic IFCs calculation, except a slightly smaller energy cutoff (520 eV) was used to reduce the computational cost.

## Lattice thermal conductivity

The calculated harmonic and anharmonic force constants were used to solve the phonon Boltzmann transport equation iteratively as implemented in the ShengBTE code.<sup>41–43</sup> The lattice thermal conductivity due to particle like transport channel ( $\kappa_p$ ) can be give as:

$$\kappa_p^{\alpha\beta} = \frac{1}{N\Omega} \sum_{\lambda} C_{\lambda} v_{\lambda,\alpha} \otimes v_{\lambda,\beta} \tau_{\lambda} \quad (1)$$

where N, and  $\Omega$  are the number of unitcells in the system and volume of the unitcell, respectively.  $C_{\lambda}$ ,  $\tau_{\lambda}$  are the specific heat and phonon lifetimes for a phonon mode  $\lambda$  with wave-vector  $\mathbf{q}$  and polarization j, respectively.  $v_{\lambda,\alpha}$  is the  $\alpha^{\text{th}}$  component of the phonon group velocity  $v_{\lambda}$ .

Convergence of  $\kappa_l$  with respect to various dependent parameters such as cut-off distance for 3<sup>rd</sup> order IFCs, Gaussian smearing width was carefully tested and the same are provided in the supporting information (Figure S1). For the calculations reported here, a Gaussian smearing width of 1.0 was used to approximate the Dirac distribution, and a q-point mesh of  $21 \times 21 \times 9$  was used for Brillouin zone integration. In these calculations, three-phonon scattering and isotopic disorder scattering<sup>44</sup> from natural isotope mass variation are considered.

The solution of Boltzmann transport equation discussed above only includes the contribution from the particle transport channel. As recently shown for strongly anharmonic materials contribution from the coherence channel

can also be significant.<sup>45–49</sup> The coherence contribution ( $\kappa_c$ ) to lattice thermal conductivity is calculated using the off diagonal terms of velocity operator<sup>50,51</sup> using the method proposed by Simoncelli and co-authors.<sup>45</sup> The  $\kappa_c$  is described as

$$\kappa_c^{\alpha\beta} = \frac{\hbar^2}{k_B T^2} \frac{1}{\Omega N_q} \sum_{\mathbf{q}} \sum_{j \neq j'} \frac{\omega_{\mathbf{q}j} + \omega_{\mathbf{q}j'}}{2} V_{\mathbf{q},\alpha}^{j,j'} \cdot V_{\mathbf{q},\beta}^{j,j'} \frac{\omega_{\mathbf{q}j} n_{\mathbf{q}j} (n_{\mathbf{q}j} + 1) + \omega_{\mathbf{q}j'} n_{\mathbf{q}j'} (n_{\mathbf{q}j'} + 1)}{4(\omega_{\mathbf{q}j'} - \omega_{\mathbf{q}j})^2 + (\Gamma_{\mathbf{q}j} + \Gamma_{\mathbf{q}j'})^2} (\Gamma_{\mathbf{q}j} + \Gamma_{\mathbf{q}j'}) \quad (2)$$

where,  $k_B$ ,  $\hbar$ ,  $\Omega$ ,  $N_q$ , and  $n_{\mathbf{q}j}$  are the Boltzmann constant, reduced Plank constant, volume of the unit cell, number of  $\mathbf{q}$  points, the Bose-Einstein distribution, respectively.  $\Gamma_{\mathbf{q}j}$  is the phonon linewidth and  $V_{\mathbf{q},\alpha}^{j,j'}$  is the  $\alpha^{\text{th}}$  component of velocity operator. The thermal conductivity results presented in the main article include contribution from both particle  $\kappa_p$ , and coherence  $\kappa_c$  channels ( $\kappa_l = \kappa_p + \kappa_c$ ). As shown in Figure S2 and S3, the contribution at room temperature, the  $\kappa_c$  varies from 0.3 W/m-K (0 GPa) to 0.16 W/m-K (20 GPa) at high pressures.

## Results and Discussion

### Crystal structure and structural phase transition

As discussed in the introduction,  $\text{Bi}_2\text{O}_2\text{S}$  crystallizes in the low symmetry ( $Pnmn$ ) structure (see Figures 1(a-b)) compared to heavy chalcogen based systems namely  $\text{Bi}_2\text{O}_2\text{Se}$  and  $\text{Bi}_2\text{O}_2\text{Te}$  at ambient conditions. This is due to the presence of stereochemically active  $6s^2$  lone pair of  $\text{Bi}^{3+}$  cation in  $\text{Bi}_2\text{O}_2\text{S}$  while its activity might be suppressed by chemical pre-compression of heavy chalcogens (Se and Te) in  $\text{Bi}_2\text{O}_2\text{Se}$  and  $\text{Bi}_2\text{O}_2\text{Te}$  systems, which drives them to crystallize in relatively higher symmetry ( $I4/mmm$ ) structure (see Figures 1(c-d)) and the  $Pnmn$  structure is distorted analogue of  $I4/mmm$  crystal structure. To investigate the bonding differences between these two phases further, we examined the ELF<sup>52,53</sup> as

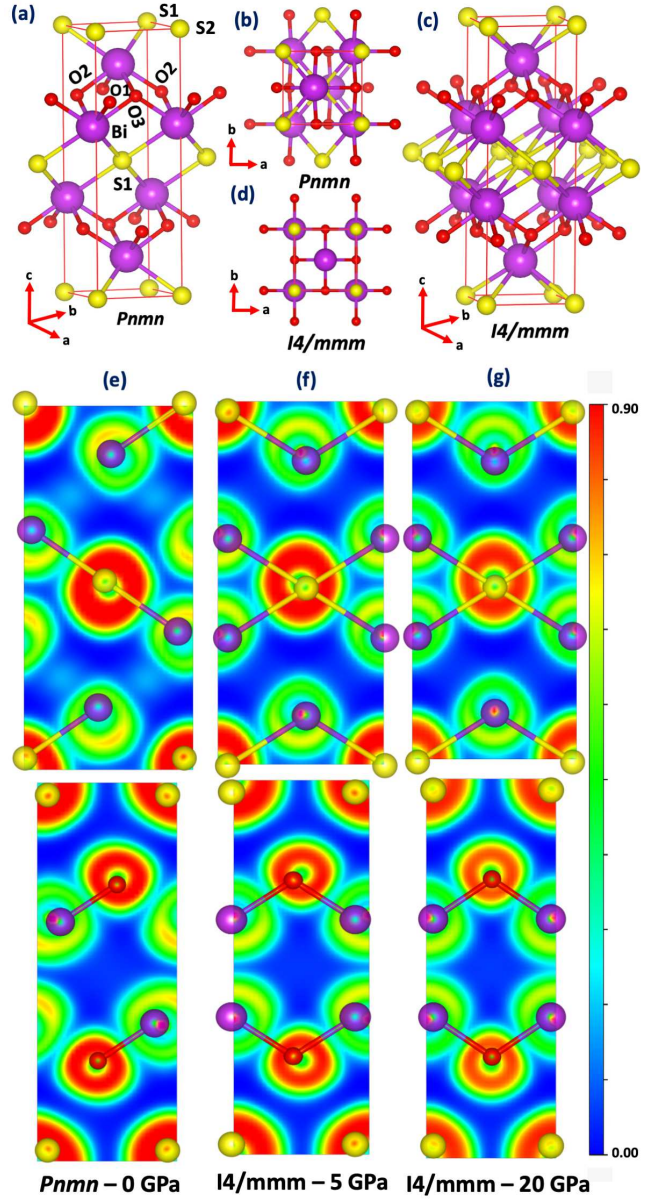


Figure 1: Crystal structure of (a) ambient ( $Pnmn$ ) phase (b) distorted crystal structure in  $ab$ -plane due to lone pair at  $\text{Bi}^{3+}$  cation (c) crystal structure of high pressure ( $I4/mmm$ ) phase and (d) ordered crystal structure in  $ab$ -plane due to centering of  $\text{Bi}^{3+}$  cation in  $I4/mmm$  phase. Calculated electron localization function (ELF) at (e) 0 GPa for  $Pnmn$  phase and (f) 5 and (g) 20 GPa for  $I4/mmm$  phase projected on the (110) plane for Bi-S bonds (middle panel) and (010) plane for Bi-O bonds (bottom panel). Red and blue ends represent high electron localization and no localization, respectively. All ELFs are plotted at an iso-surface value of  $0.005 \text{ e}/\text{\AA}^3$ .

depicted in Figures 1(e)-(g). The ELF is projected onto the (110) and (010) planes, which contain Bi, S and Bi, O atoms, respectively. The red color represents complete electron localization, while the blue color represents almost no electron localization.

The ELF of the two phases appear similar at first glance, but significant differences can be seen around Bi-S and Bi-O bonds. In the  $Pnmn$  phase, the  $\text{Bi}^{3+}$  cation lone pair can be seen by yellow lobe regions of electron localization in Figure 1(e). When the pressure is applied (Figures 1(f)-(g)), the intensity of the yellow lobes surrounding the  $\text{Bi}^{3+}$  cation is significantly reduced, indicating that the lone pair of  $\text{Bi}^{3+}$  cation is being suppressed. Due to presence of lone pair in  $Pnmn$  phase, the coordination environment around  $\text{Bi}^{3+}$  cation differs greatly between these two phases. In  $Pnmn$  phase, Bi and S have two in-equivalent bond lengths and these are listed as Bi-S1 (3.00 Å) and Bi-S2 (3.51 Å) in Table S1 and Figure 1(a). While in the  $I4/mmm$  phase, Bi and S bonds have four-fold coordination with only one in-equivalent bond with a length of 3.14 Å. Similarly, the bond length between Bi and O atoms in the  $Pnmn$  phase ranges from 2.24 to 2.43 Å (Bi-O1, Bi-O2 and Bi-O3 as shown in Table S1 and Figure 1(a)), whereas in the  $I4/mmm$  phase, all Bi-O bonds are identical, with a bond length of 2.19 Å. Overall, the bonding is highly heterogeneous in the  $Pnmn$  phase over  $I4/mmm$  phase.

A recent HP-XRD study<sup>26</sup> revealed that  $\text{Bi}_2\text{O}_2\text{S}$  undergoes a structural phase transition from orthorhombic ( $Pnmn$ ) to tetragonal ( $I4/mmm$ ) structure at 6.4 GPa due to dynamic cation centering and then it transforms from 2D to 3D structure upon further compression above 13.2 GPa because of complete suppression of the  $6s^2$  lone pair of  $\text{Bi}^{3+}$  cation. To get further insights on structural phase transition and anharmonicity, we have systematically investigated the high pressure behavior of  $\text{Bi}_2\text{O}_2\text{S}$  up to 20 GPa. As shown in Figure 2(a), the enthalpy difference between ambient and high pressure phases is gradually decreasing with pressure up to 3 GPa and there after both phases exhibit iso-enthalpic nature

above 4 GPa. This result suggests a 2<sup>nd</sup> order phase transition from  $Pnmn \rightarrow I4/mmm$  in  $\text{Bi}_2\text{O}_2\text{S}$ . To gain further insights on the structural phase transition, we analyze the pressure dependent lattice constants, bond parameters as a function of pressure and equation of state (EOS). As shown in Figure 2(b), the calculated volumes for both  $Pnmn$  and  $I4/mmm$  phases are converging and become almost equal above 3 GPa until the maximum studied pressure range (0-20 GPa) in this work and it is in excellent agreement with the HP-XRD measurements.<sup>26</sup> No volume reduction is observed at the transition pressure which corroborates with iso-enthalpic nature of ambient and high pressure phases above 4 GPa. The calculated lattice constants decrease monotonically with increasing pressure. A slightly distinct variation of lattice constants above 10 GPa is observed from the HP-XRD measurements.<sup>26</sup> Interestingly, the lattice constants  $a$  and  $b$  merge into a single lattice constant above 4 GPa and lattice constant  $c$  merges into  $c$  lattice constant for high pressure tetragonal ( $I4/mmm$ ) phase (see Figure 2(c,d)). This observation is consistent with the variation of lattice constants as a function of pressure as observed in the HP-XRD measurements.<sup>26</sup> The calculated pressure coefficients by fitting the pressure versus lattice parameter data to a quadratic expression show that the  $Pnmn$  lattice is highly compressible along a-crystallographic direction, which is consistent with the obtained low elastic moduli along the x-axis.

As illustrated in Figure S4 and S5, the calculated in-equivalent bond lengths (Bi-S and Bi-O) and angles (S-Bi-S and O-Bi-O) of lower symmetry ambient  $Pnmn$  phase converge and merge into a single in-equivalent bond length/angle for higher symmetry  $I4/mmm$  phase above 4 GPa. From HP-XRD measurements,<sup>26</sup> above 13.2 GPa, a sharp reduction of Bi-S and increase of Bi-O bonds have been observed due complete suppression of lone pair thus resulting in  $I4/mmm$  structure to be transformed from 2D to 3D. However, such a sharp reduction in Bi-S and increase in Bi-O bond lengths are not observed using static first principles calculations under high pressure, in-

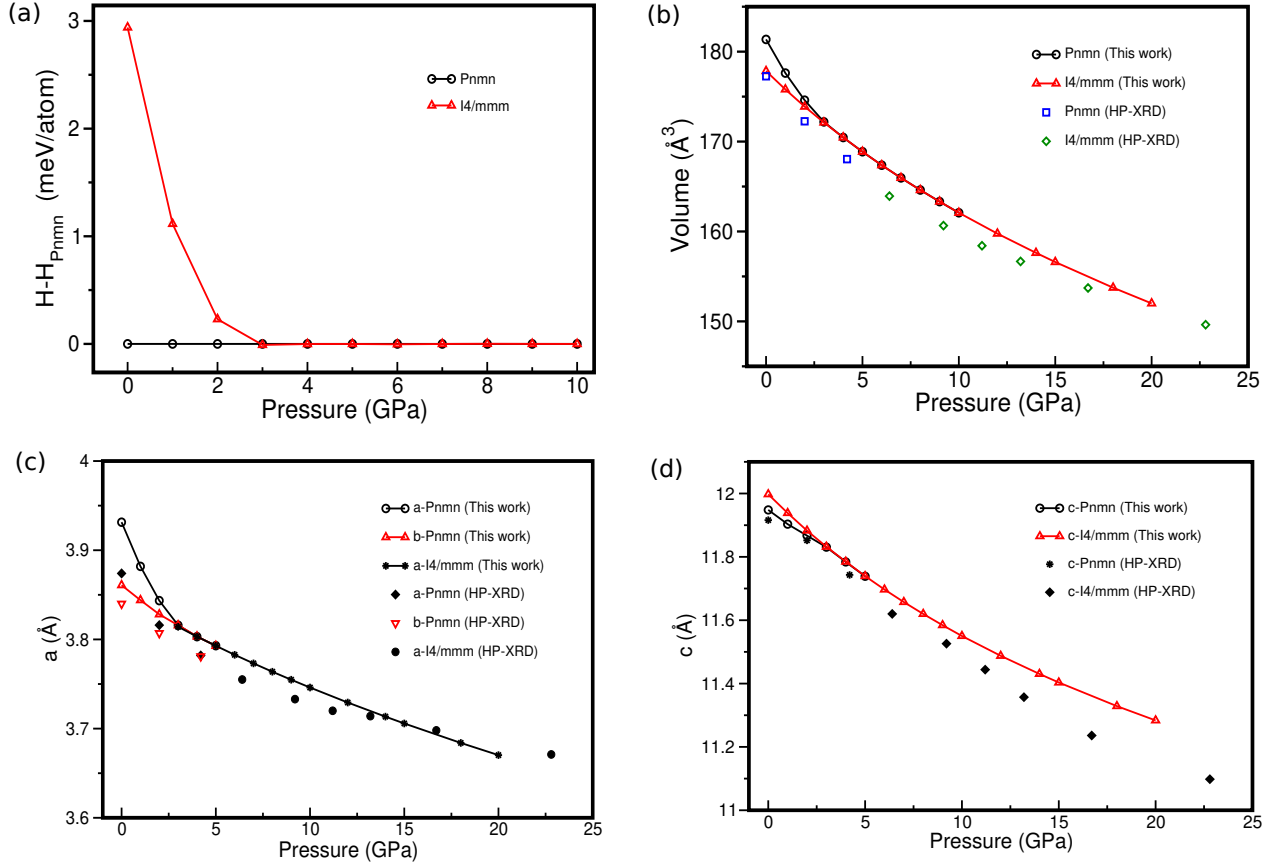


Figure 2: (a) Relative enthalpy difference of high pressure ( $I4/mmm$ ) phase w.r.t ambient ( $Pnmm$ ) phase. Pressure dependent (b) volume ( $V$ ) (c, d) lattice constants ( $a$ ,  $c$ ) of ambient ( $Pnmm$ ) and high pressure ( $I4/mmm$ ) phases of  $\text{Bi}_2\text{O}_2\text{S}$  are compared with the lattice constants and volume determined from the HP-XRD measurements.<sup>26</sup>

stead these bond lengths are monotonically decreasing with pressure (Figure S4). This indicates that the lone pair of  $\text{Bi}^{3+}$  cation was not completely suppressed until 20 GPa, This result is consistent with a combined study<sup>26</sup> of HP-XRD and first principles calculations, where a relatively small activity of the lone pair for  $I4/mmm$  phase could be seen at 22.8 GPa although lone pair was completely suppressed at 13.2 GPa from HP-XRD measurements of the same study. The possible reasons for the distinct behavior of static first principles calculations and HP-XRD measurements might be 1) HP-XRD measurements were performed using Neon as pressure transmitting medium,<sup>26</sup> which might create a quasi-hydrostatic or non-hydrostatic conditions above 13 GPa.<sup>54</sup> 2) Anharmonic effects are not considered for computation of structural properties under high

pressure whereas HP-XRD measurements were carried out at 300 K.<sup>26</sup> The static enthalpy calculations and pressure evolution of structural properties of ambient and high pressure phases clearly demonstrate that  $\text{Bi}_2\text{O}_2\text{S}$  undergoes a continuous phase transition from  $Pnmm \rightarrow I4/mmm$  under high pressure due to displacive nature of the off centred  $\text{Bi}^{3+}$  cation (Figure S6) which removes the lattice distortion and probing high pressure phase to crystallizes in high symmetry structure under hydrostatic compression.

To gain further insights into bonding changes under pressure we then analyze the projected CHOP (pCOHP) for various Bi-O and Bi-S bonds for both ambient and high pressure phases. Figures 3 (a)-(d) shows the pCHOP for in-equivalent bonds of  $Pnmm$  and  $I4/mmm$  phases as a function of pressure. There are

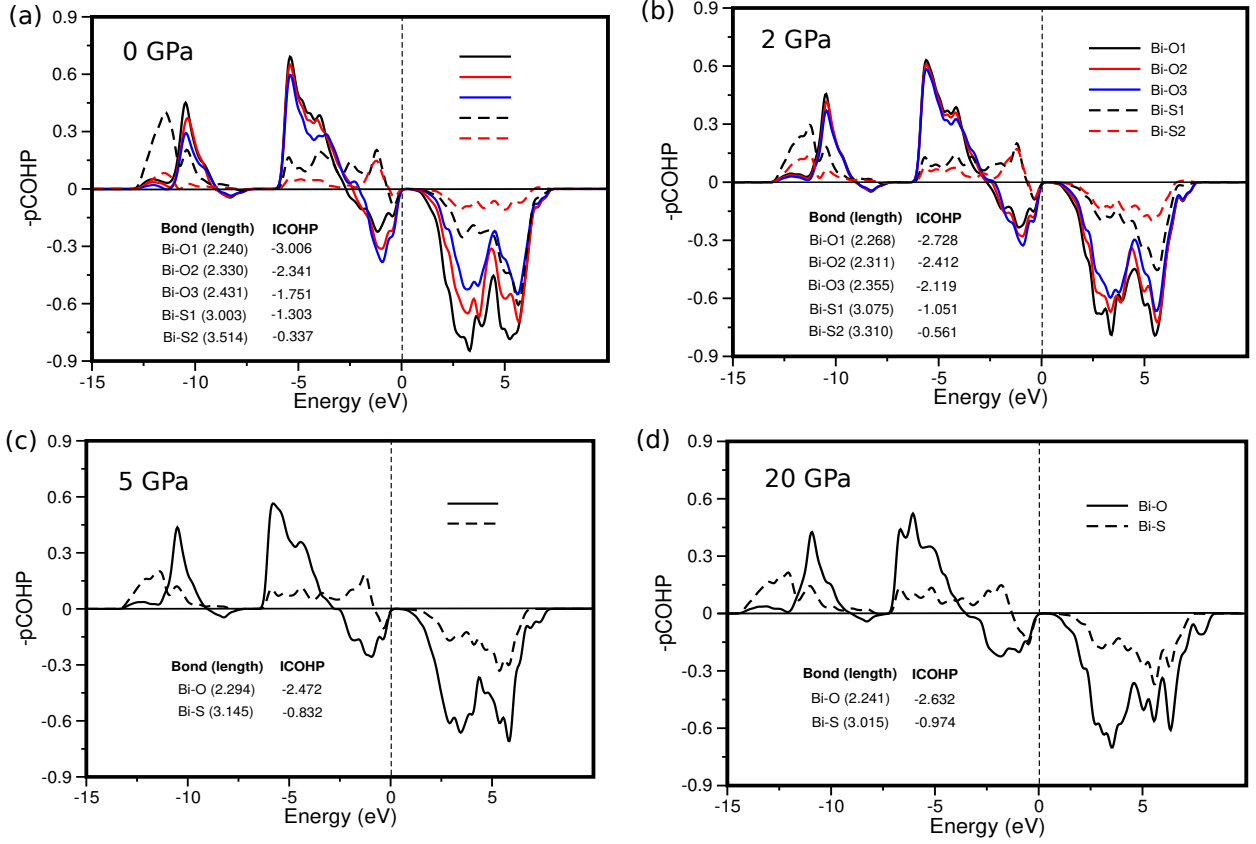


Figure 3: Projected crystal orbital Hamiltonian population (pCOHP) at (a) 0 GPa and (b) 2 GPa for *Pnmn* phase and at (c) 5 GPa and (d) 20 GPa for *I4/mmm* phase. The integrated COHP values are given at each pressure for both *Pnmn* and *I4/mmm* phases which show the variation of strength of the bonds as a function pressure as shown in Figure S7. The bonding states are positive and anti-bonding states are negative. Bond lengths are given in Å and ICOHP values provided in eV

significant anti-bonding states for Bi-O bonds compared to Bi-S bonds above and near the Fermi level. Relatively, the anti-bonding states in *I4/mmm* phase are stabilizing with pressure compared to the ambient *Pnmn* phase. The integrated COHP (ICOHP) analysis show that the *Pnmn* phase consists of mixed strong (more negative ICOHP value indicates stronger bonding) and weak (less ICOHP negative value indicates weaker bonding) bonds of Bi-O and Bi-S at ambient pressure (Figure S7). Especially, Bi-S2 shows a relatively weaker bonding nature resulting in rattling behavior as shown from the atomic mean square displacements, which favours strong anahrmnicity thus lowering the  $\kappa_l$ .

## Electronic structure and Born effective charges

It is well-known fact that the standard DFT functionals underestimate the band gaps<sup>55,56</sup> by 30-40 % for semiconductors and insulators due to self-interaction error (SIE), to overcome SIE problem, we have used TB-mBJ<sup>36</sup> potential to calculate electronic structure of Bi<sub>2</sub>O<sub>2</sub>S. The calculated band gaps are 0.78 and 0.60 eV without and with inclusion of spin-orbit coupling (SOC) within PBE-GGA, respectively for *Pnmn* phase and the corresponding band gaps obtained using TB-mBJ potential are 1.55 and 1.45 eV. The obtained PBE-GGA band gap 0.78 eV without SOC is comparable with previously obtained band gap of 1.0 eV,<sup>17</sup> and the TB-mBJ band gap with SOC 1.45 eV is con-

Table 2: Calculated enhanced Born effective charges ( $Z^*$ ) of ambient ( $Pn\bar{m}n$ ) and high pressure ( $I4/m\bar{m}m$ ) phases of  $\text{Bi}_2\text{O}_2\text{S}$ .

Atom	Formal charge	$Z^*(Pn\bar{m}n)$	$Z^*(I4/m\bar{m}m)$
Bi	+3	$\begin{pmatrix} 5.34 & 0.00 & 0.19 \\ 0.00 & 5.89 & 0.00 \\ 0.54 & 0.00 & 5.19 \end{pmatrix}$	$\begin{pmatrix} 5.83 & 0.00 & 0.00 \\ 0.00 & 5.83 & 0.00 \\ 0.00 & 0.00 & 5.24 \end{pmatrix}$
O	-2	$\begin{pmatrix} -3.55 & 0.00 & 0.58 \\ 0.00 & -3.73 & 0.00 \\ 0.10 & 0.00 & -3.61 \end{pmatrix}$	$\begin{pmatrix} -3.69 & 0.00 & 0.00 \\ 0.00 & -3.69 & 0.00 \\ 0.00 & 0.00 & -3.71 \end{pmatrix}$
S	-2	$\begin{pmatrix} -3.57 & 0.00 & 0.37 \\ 0.00 & -4.31 & 0.00 \\ 0.94 & 0.00 & -3.15 \end{pmatrix}$	$\begin{pmatrix} -4.28 & 0.00 & 0.37 \\ 0.00 & -4.28 & 0.00 \\ 0.94 & 0.00 & -3.05 \end{pmatrix}$

sistent with HSE06 band gap of 1.25 eV.<sup>15</sup> As shown by Shi et al.,<sup>57</sup> materials with fully occupied lone pair ( $ns^2$ ,  $n = 4, 5, 6$ ) show distinct features in their electronic structure by having an additional band (dominated by fully occupied cation  $s$ -states) below the valence band compared to the materials without lone pair cation. The conduction band is mainly dominated by extended  $p$ -states of lone pair cation in contrast to the cation  $s$ -states in materials without lone pair cation. The calculated projected electronic density of states (PDOS) for both ambient orthorhombic and high pressure tetragonal (at 5 GPa, 10 GPa and 20 GPa) phases of  $\text{Bi}_2\text{O}_2\text{S}$  are presented in Figure S8. The band profiles look similar for ambient and high pressure phases at 0 GPa and 5 GPa, respectively. As discussed above, the bottom of the valence band is mainly derived from  $6s$ -states of  $\text{Bi}^{3+}$  cation for both of these phases ( $Pn\bar{m}n$  and  $I4/m\bar{m}m$ ). As shown in Figure S8, the top of the valence band is mainly dominated by the  $p$ -states of  $\text{S}^{2-}$  and  $\text{O}^{2-}$  anions and also minor contribution from  $s$  and  $p$ -states of the  $\text{Bi}^{3+}$  cation, while the conduction band is mainly dominated by extended  $p$ -states of the  $\text{Bi}^{3+}$  cation, which hybridize with anion ( $\text{S}^{2-}$  and  $\text{O}^{2-}$ )  $p$ -states of the valence band, thus, results in a mixed ionic-covalent character which causes a significant cross-band-gap hybridization in  $\text{Bi}_2\text{O}_2\text{S}$ . The observed mixed ionic-covalent character causes strong lattice polarization for the lone pair cation containing compounds.<sup>58,59</sup> This could be clearly seen from Born effective charges (BECs), as presented in

Table 2, the calculated BECs are significantly enhanced for both phases of  $\text{Bi}_2\text{O}_2\text{S}$  compared to the formal charges of cation (+3) and anions (-2). Enhanced BECs provide large LO-TO splitting from phonon dispersion curves which brings the lattice (TO modes) in the proximity of ferroelectric instability<sup>58</sup> thereby lowering  $\kappa_l$ .<sup>60</sup> Therefore, it is very intriguing to investigate elastic and phonon transport properties of stereochemically active lone pair materials under hydrostatic compression in general and in particular for  $\text{Bi}_2\text{O}_2\text{S}$ .

## Mechanical and dynamical stability

To explore the mechanical and dynamical stability, we calculated second order elastic constants (SOECs) and phonon dispersion curves, respectively for  $Pn\bar{m}n$  and  $I4/m\bar{m}m$  phases of  $\text{Bi}_2\text{O}_2\text{S}$  at ambient as well as at high pressure. The calculated SOECs at 0 and 5 GPa for both the phases are given in Table 3. At 0 GPa, the  $Pn\bar{m}n$  phase obeys necessary and sufficient conditions of Born stability criteria<sup>61</sup> and no imaginary frequencies are observed, which indicate that the  $Pn\bar{m}n$  phase is mechanically and dynamically stable at ambient pressure (see Figure 4(a)). The  $I4/m\bar{m}m$  phase doesn't satisfy the Born stability criteria ( $C_{44} > 0$ ) and also it possesses imaginary frequencies along  $\Gamma$ -M direction (see Figure 4(b)) at 0 GPa, which clearly demonstrate that  $I4/m\bar{m}m$  phase is mechanically and dynamically unstable at ambient



pressure which clearly demonstrates that role stereochemical activity of the lone pair in determining the stability of  $Pn\bar{m}n$  phase at ambient pressure for  $\text{Bi}_2\text{O}_2\text{S}$ .

When a non-zero hydrostatic pressure is applied to a particular crystal system, the Born stability criteria must be revised with modified elastic constants at a given hydrostatic pressure ( $P$ ) conditions. According to Sinko and Smirnov<sup>62,63</sup> the modified elastic constants at a given pressure are  $\tilde{C}_{ii} = C_{ii} - P$ , (for  $i = 1-6$ ) and  $\tilde{C}_{12} = C_{12} + P$ ,  $\tilde{C}_{13} = C_{13} + P$  and  $\tilde{C}_{23} = C_{23} + P$ . Therefore, the modified Born stability criteria under hydrostatic pressure for orthorhombic crystal symmetry can be found in our previous work,<sup>64</sup> whereas for tetragonal system the same are given as follows:

$$\begin{aligned} C_{11} - C_{12} - 2P > 0; C_{44} - P > 0 \\ P^2 + P(C_{11} + C_{12} + 4C_{13}) \\ + 2C_{13}^2 - C_{33}(C_{11} + C_{12}) > 0; C_{66} - P > 0 \end{aligned} \quad (3)$$

Under high pressure ( $> 4$  GPa), for instance at 5 GPa (see Table 3), the calculated SOECs for both  $Pn\bar{m}n$  and  $I4/m\bar{m}m$  phases have the following relationships:  $C_{11}^{Pn\bar{m}n} \approx C_{22}^{Pn\bar{m}n} \approx C_{11}^{I4/m\bar{m}m}$ ,  $C_{44}^{Pn\bar{m}n} = C_{55}^{Pn\bar{m}n} = C_{44}^{I4/m\bar{m}m}$  and  $C_{12}^{Pn\bar{m}n} \approx C_{13}^{Pn\bar{m}n} = C_{12}^{I4/m\bar{m}m}$ . These relationships strongly suggest a continuous phase transition from  $Pn\bar{m}n$  to  $I4/m\bar{m}m$  is occurring due to displacive nature of  $\text{Bi}^{3+}$  cation in  $\text{Bi}_2\text{O}_2\text{S}$  with increasing pressure (Figure S6) and is in good accord with the pressure dependent structural properties such as pressure dependent lattice constants and bond parameters (Figures 2, S3 and S4). In addition, no imaginary frequencies are found for the computed phonon dispersion curves at 5 GPa, which strongly suggest that  $I4/m\bar{m}m$  phase becomes dynamically stable above 5 GPa (Figure S9).

## Lattice dynamics and phonon transport

In general, the lone pair electrons are shown to favor low lattice thermal conductivity,<sup>4,65</sup> and the pressure tunability of lone pair activity can

have important implications for  $\kappa_l$ . To investigate this further, we analyze the lattice dynamics and phonon transport of  $\text{Bi}_2\text{O}_2\text{S}$  as a function of pressure within the 0-20 GPa pressure range. Note that below 5 GPa pressure,  $\text{Bi}_2\text{O}_2\text{S}$  has orthorhombic  $Pn\bar{m}n$  structure and at higher pressure it transforms to tetragonal  $I4/m\bar{m}m$  structure. Therefore, at low pressure (0, and 2 GPa)  $\kappa_l$  calculations are performed for  $Pn\bar{m}n$  structure, whereas at high pressure ( $\geq 5$  GPa)  $\kappa_l$  calculations are done for  $I4/m\bar{m}m$  structure. The calculated phonon dispersion curves and phonon density of states (PHDOS) are shown in Figures 4(a) and (b) for 0 GPa ( $Pn\bar{m}n$ ) and 5 GPa ( $I4/m\bar{m}m$ ) phases, respectively. Phonon dispersion for other pressure values are shown in the supporting information Figure S9. For both  $Pn\bar{m}n$  and  $I4/m\bar{m}m$  phases, the three acoustic modes are comprised of very low frequencies ( $\leq 1.5$  THz) and they overlap with optical branches. In both the phases, the optical phonons show very low frequency modes due to presence of heavy metal Bi and they hybridize with the acoustic phonon modes. The optical phonon branches in high-frequency regions ( $> 6$  THz) are dispersive and exhibit large phonon group velocity, indicating the possibility of contribution to  $\kappa_l$ . The PHDOS in these compounds can be divided into three main regions: Bi dominated region below 1 THz, mixed Bi and S region above 1 THz, and O dominated region above 6 THz. Despite the huge mass contrast between Bi and S ( $m_{\text{Bi}}/m_{\text{S}} = 6.5$ ), there is a significant overlap between Bi and S in the PHDOS. This overlap is larger for the  $Pn\bar{m}n$  phase (1 THz - 5.5 THz) than in the  $I4/m\bar{m}m$  phase (3 THz - 5.5 THz). The sulfur PHDOS in the  $Pn\bar{m}n$  phase shows several small peaks in 1 THz - 5.5 THz and a large peak around 5 THz. The  $I4/m\bar{m}m$  phase also shows sulfur peaks in the PHDOS, but these are less pronounced. The large overlap between acoustic and optical phonons can lead to enhanced scattering of the heat-carrying acoustic phonons — suggesting the possibility of relatively low  $\kappa_l$  for the  $Pn\bar{m}n$  phase.

The temperature-dependent  $\kappa_l$  at various pressures is compared in Figure 5(a) and (b) along in-plane and cross-plane directions.

Table 3: Calculated second order elastic constants (in GPa) of ambient ( $Pn\bar{m}n$ ) and high pressure ( $I4/m\bar{m}m$ ) phases of  $\text{Bi}_2\text{O}_2\text{S}$  at 0 and 5 GPa.

Phase	Pressure	$C_{11}$	$C_{22}$	$C_{33}$	$C_{44}$	$C_{55}$	$C_{66}$	$C_{12}$	$C_{13}$	$C_{23}$
$Pn\bar{m}n$	0.0	57.8	126.0	119.5	16.6	27.8	22.1	24.7	23.4	28.3
$I4/m\bar{m}m$	0.0	160.5	160.5	139.4	-6.79	-6.79	60.5	74.0	41.0	41.0
$Pn\bar{m}n$	5.0	189.4	189.0	184.9	14.7	14.7	72.6	96.6	57.1	57.3
$I4/m\bar{m}m$	5.0	188.3	188.3	184.0	14.7	14.7	72.6	95.8	57.8	57.8

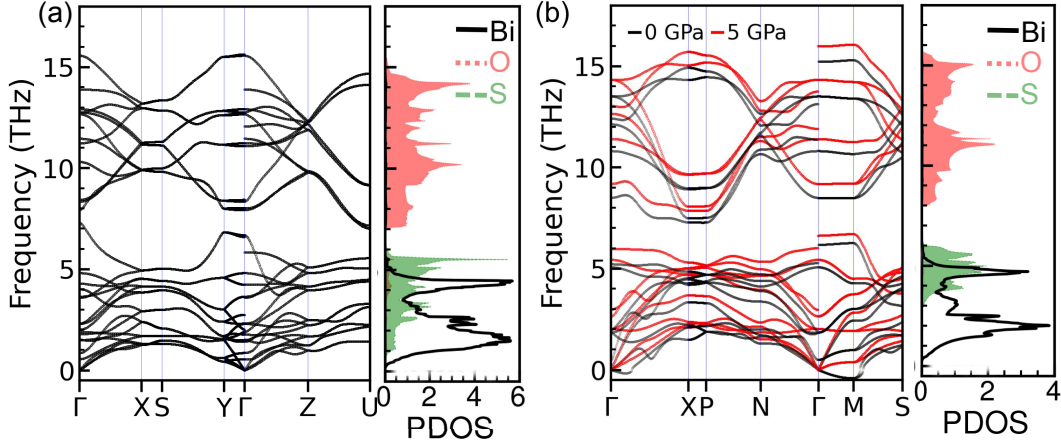


Figure 4: Phonon dispersion curves and density of states for  $\text{Bi}_2\text{O}_2\text{S}$  in (a) ambient ( $Pn\bar{m}n$ ) and (b) high pressure ( $I4/m\bar{m}m$ ) phases. For  $I4/m\bar{m}m$  phase, the 0 GPa phonon dispersion is also shown. As can be seen under applied pressure,  $I4/m\bar{m}m$  phase becomes dynamically stable.

As can be seen there,  $\kappa_l$  of the ambient  $Pn\bar{m}n$  phase is smaller than the high pressure  $I4/m\bar{m}m$  phase. At room temperature, the average  $\kappa_l$  values are 1.71, 4.92 W/m-K and 12.65 W/m-K for  $Pn\bar{m}n$  (0 GPa),  $I4/m\bar{m}m$  (5 GPa), and  $I4/m\bar{m}m$  (20 GPa) phase, respectively. The calculated 300 K lattice thermal conductivity values ( $\kappa_l^{\parallel} = 2.02$  W/m-K;  $\kappa_l^{\perp} = 1.046$  mW/m-K) for the ambient phase are somewhat smaller than the ones reported ( $\kappa_l^{\parallel} = 2.93$  W/m-K;  $\kappa_l^{\perp} = 1.7$  W/m-K) in a previous study.<sup>66</sup> This difference largely stems from different lattice parameters (due to different in DFT functional), and different cutoffs used for calculations of 3<sup>rd</sup> order IFCs. At 2 GPa hydrostatic pressure the in-plane lattice parameters are similar to the ones reported in reference,<sup>66</sup> and the calculated lattice thermal conductivity ( $\kappa_l^{\parallel} = 3.13$  W/m-K, and  $\kappa_l^{\perp} = 1.75$  W/m-K) is in better agreement with previously reported values.<sup>66</sup> When compared with the  $\kappa_l$  of with other dibismuth dioxychalcogenides such as  $\text{Bi}_2\text{O}_2\text{Se}$ <sup>20</sup> ( $\kappa_l^{\parallel} = 1.71$  W/m-K;  $\kappa_l^{\perp} = 0.81$

W/m-K at 300 K) the calculated room temperature  $\kappa_l$  for the ambient  $\text{Bi}_2\text{O}_2\text{S}$  are a bit higher. This difference in  $\kappa_l$  originates from the lower group velocity induced by relatively heavier Se atom in  $\text{Bi}_2\text{O}_2\text{Se}$ . Nonetheless the  $\kappa_{\perp}$  of ambient  $\text{Bi}_2\text{O}_2\text{S}$  are comparable with well known bismuth chalcogenides thermoelectric materials such as,  $\text{Bi}_2\text{Te}_3$ ,<sup>67</sup>  $\text{Bi}_2\text{Se}_3$ ,<sup>20,68</sup> and  $\text{Bi}_2\text{S}_3$ .<sup>69,70</sup>

Since both  $Pn\bar{m}n$  and  $I4/m\bar{m}m$  phases have an anisotropic crystal structure, the same is reflected in the calculated  $\kappa_l$ . Due to the orthorhombic structure, the  $Pn\bar{m}n$  phase exhibits slightly different  $\kappa_l$  along in-plane  $x$  (2 W/m-K) and  $y$  (2.12 W/m-K) directions. Upon application of pressure as the  $a$  and  $b$  lattice parameters converge to single value,  $\kappa_l$  along in-plane  $x$  and  $y$  direction also becomes same (Figure S2 (b)). Upon further application of pressure, the pressure  $\geq 5$  GPa,  $\kappa_l$  becomes identical along  $x$  and  $y$  directions (Figure S2 (c)). As expected for layered materials with weak electrostatic interactions,<sup>20</sup> the  $\kappa_l$  along the cross-plane direction is smaller than the in-plane di-

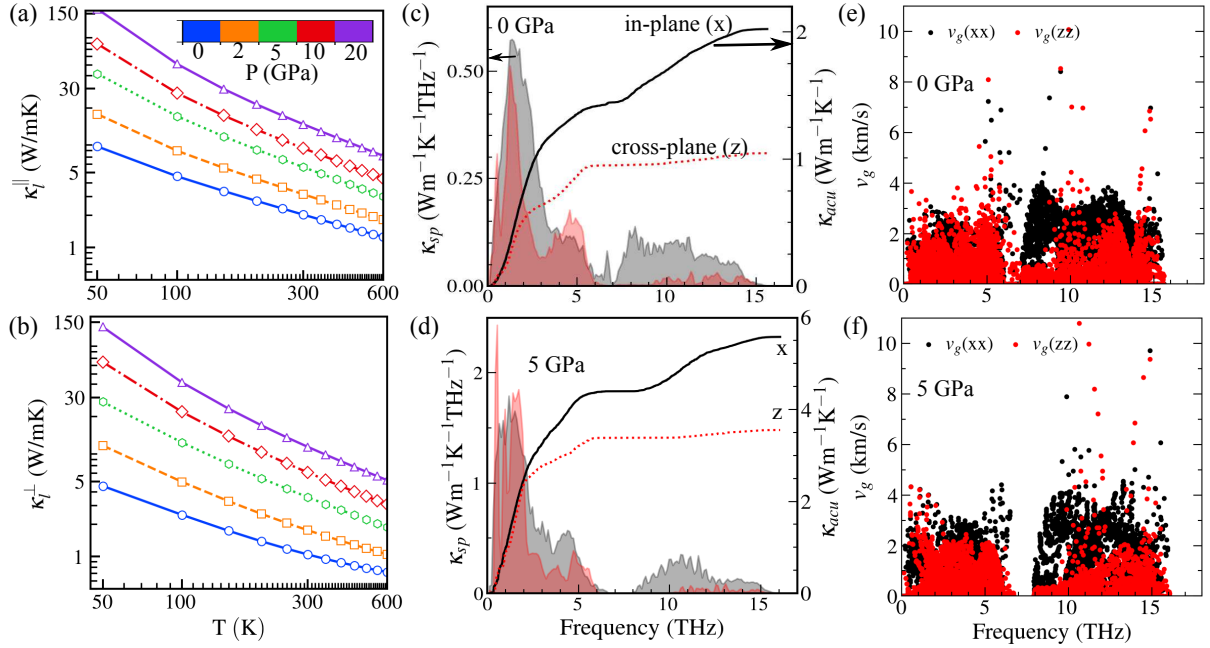


Figure 5: Comparison of calculated  $\kappa_l$  as a function of temperature for ambient and 2 GPa  $Pn\bar{m}n$  and high pressure 5, 10 and 20 GPa  $I4/m\bar{m}m$  phases of  $\text{Bi}_2\text{O}_2\text{S}$  along (a) in-plane ( $\parallel$ ) and cross-plane ( $\perp$ ) directions. Calculated room temperature spectral thermal conductivity  $\kappa_{sp}$  (shaded areas) and thermal conductivity accumulation  $\kappa_{acu}$  (curves) as a function of phonon frequencies at (c) 0 GPa and (d) 5 GPa. In plane (xx) and cross plane (zz) components of phonon group velocities as a function of frequencies at (e) 0 GPa and (f) 5 GPa.

rection. Interestingly, the calculated thermal transport anisotropy is much smaller than what is typically observed in vdW layered materials such as,  $\text{MoS}_2$  where  $\kappa_l^{\parallel}/\kappa_l^{\perp}$  of nearly 30 was found.<sup>21</sup> This clearly distinguishes difference between the role of interlayer weak electrostatic and vdW bonding in determining the thermal anisotropy within the layered materials.

To understand the thermal transport behavior further we calculate the cumulative  $\kappa_{acu}$  and spectral  $\kappa_{sp}$  lattice thermal conductivity as a function of phonon frequency, which is shown in Figure 5(c) and (d) for  $Pn\bar{m}n$  and  $I4/m\bar{m}m$  phases. As can be seen there, in both the phases, the optical phonons contribute significantly to  $\kappa_l$  particularly along the in-plane direction. The phonon frequency range contributing to cross-plane and in-plane  $\kappa_l$  is also quite different. The  $\kappa_l^{\perp}$  is mostly originates from phonons with frequency  $< 5$  THz, whereas phonons with frequencies up to 12 THz contribute to  $\kappa_l^{\parallel}$  in both the phases. This can be understood by analyzing phonon group veloci-

ties which are shown in the Figure 6(e) and (f) for  $Pn\bar{m}n$  and  $I4/m\bar{m}m$  phases, respectively. In both the phases for the majority of the frequency range  $v_g$  is higher along in-plane (xx) direction than the cross-plane (zz) direction. This is more prominent for optical phonons in the frequency window of 6-12 THz, where in-plane  $v_g$  is more than two times larger than the cross-plane  $v_g$ . These higher in-plane  $v_g$  values are the main reason for higher  $\kappa_l$  along the in-plane direction. This is true for all the pressures investigated here as shown in Figure S10.

We then focus on exploring the origin of the relatively low  $\kappa_l$  in the  $Pn\bar{m}n$  phase. To explain the calculated differences in  $\kappa_l$ , we look into three factors, phonon group velocity, specific heat, and three phonon scattering rates, that determine  $\kappa_l$ . As explained above, the phonon group velocities (Fig. 5 (e) and (f)) are comparable in both phases — therefore phonon velocities are not the reason for the lower  $\kappa_l$  in the  $Pn\bar{m}n$  phase. As per the second-factor specific heat, the  $Pn\bar{m}n$  phase has only slightly higher ( $\sim 1.3\%$ ) specific heat than the

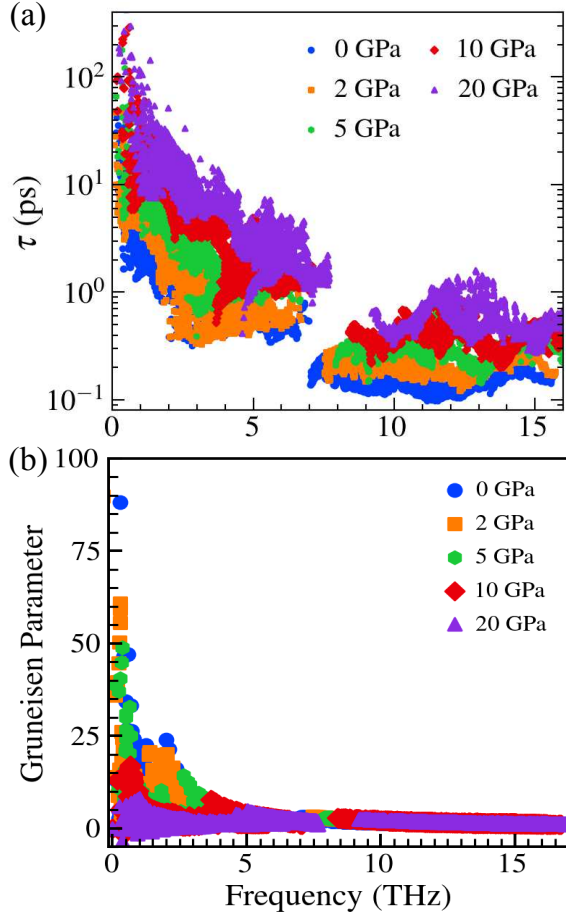


Figure 6: (a) Comparison of room temperature phonon lifetime ( $\tau$ ) for ambient (0 and 2 GPa,  $Pnmm$ ) and high pressure (5, 10 and 20 GPa  $I4/mmm$ ) phase as a function of phonon frequencies. (b) Variation of room temperature Grüneisen parameter as a function of phonon frequencies at selected pressures.

$I4/mmm$  phase. This indicates that the difference in phonon anharmonicity should be the main reason for different  $\kappa_l$ . The phonon anharmonicity governs the strength of phonon-phonon interactions which determines the overall intrinsic thermal resistance. Greater anharmonicity results in shorter phonon lifetimes and lower  $\kappa_l$ . Indeed, as shown in Figure 6(a), the phonon lifetimes of the  $Pnmm$  phase are significantly smaller than the 5 GPa  $I4/mmm$  phase over the entire frequency. The optical phonons in  $Pnmm$  phase are more dispersive than in  $I4/mmm$  phase, which enables it to satisfy the conservation laws required for three phonon scattering resulting in higher scattering phase space and therefore shorter phonon

lifetimes. With increasing pressure the phonon lifetimes continue increasing, resulting in enhancement  $\kappa_l$  with pressure. This is also consistent with the calculated Grüneisen parameters which also decrease with increasing pressure (Figure 6(b)) — signifying reduction in anharmonicity.

Both  $\kappa_l^{\parallel}$  and  $\kappa_l^{\perp}$  monotonically increase with applied pressure, and at 20 GPa, the room temperature  $\kappa_l$  becomes —  $\kappa_l^{\parallel} = 14$  W/m-K and  $\kappa_l^{\perp} = 10.5$  W/m-K. This increase of  $\kappa_l$  with pressure is mainly driven by enhancement of phonon lifetimes under pressure (Fig. 6 (a)) as the enhancement on both in-plane and cross-plane phonon group velocity due to applied pressure is rather small (Figure S10).  $\kappa_l$  anisotropy ( $\kappa_l^{\parallel}/\kappa_l^{\perp}$ ) also reduces with applied pressure from 1.94 (0 GPa) to 1.3 (20 GPa) at 300 K (Figure S11). This reduction in  $\kappa_l$  anisotropy indicates enhanced inter layer interactions, which is in good agreement with the recent HP-XRD experiments.<sup>26</sup>

As discussed earlier, the main difference between orthorhombic  $Pnmm$  and tetragonal  $I4/mmm$  phases is the suppression of  $\text{Bi}^{3+} 6s^2$  lone pair electrons in the  $I4/mmm$  phase, which may explain its relatively less anharmonicity. To gain further insights into the role of lone pair electrons in bonding and anharmonicity, we next calculate the potential energy by off-centering the Bi, O, and S atoms along Cartesian x and z directions. The resulting potential energy plots are presented in Figures 7(a) and (b) for  $Pnmm$  and  $I4/mmm$  phases, respectively. As can be seen there, the displacement potential energy of Bi and S atoms are significantly different along x and z directions in both  $Pnmm$  and  $I4/mmm$  phases. We find that for Bi and S atomic displacements in the x or y directions, the potential energy curve is relatively flat, whereas displacement along z-direction requires more energy. In both phases the energy required for O displacement is comparable.

The potential energy analysis stipulates that Bi and S vibrational modes could be easily excited by low energy. This is consistent with the calculated PHDOS, and PHDOS of Bi and S atoms show significant overlap despite huge

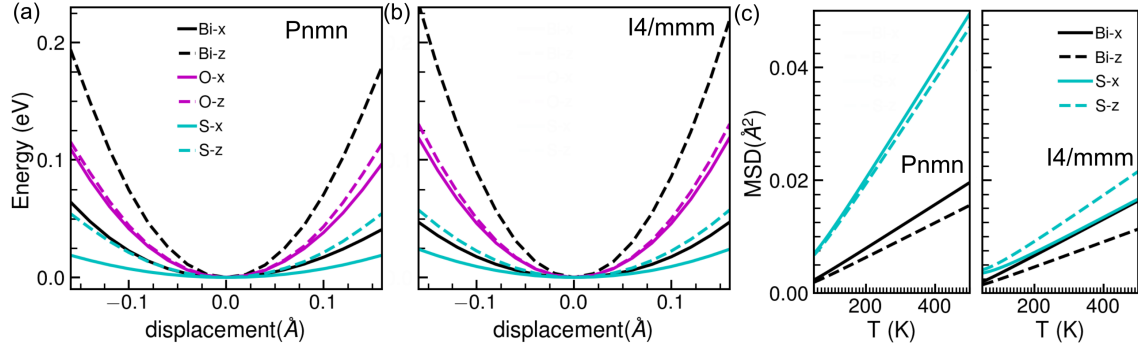


Figure 7: Average potential energy with respect to displacements of Bi, O and S atoms along Cartesian x and y directions in (a)  $Pnmn$  and (b)  $I4/mmm$  phases of  $Bi_2O_2S$ . (c) calculated average mean square displacements along Cartesian x and y directions for Bi and S atoms in both  $Pnmn$  and  $I4/mmm$  phase as a function of temperature. As can be seen mean square displacements are significantly larger for  $Pnmn$  phase.

mass difference. Furthermore, for Bi vibration in  $Pnmn$  phase potential energy curve shows asymmetric features and deviates from parabolic (harmonic) behavior. The polynomial fit of this potential energy well gives anharmonic coefficient as 2.99 and 1.68 along x and z directions, respectively. Such large deviation from typical parabolic behavior corroborates the strong anharmonicity of this phase. For comparison, in  $I4/mmm$  phase the anharmonic coefficients for Bi atomic vibrations along z direction is 1.56, and for Bi displacement along x direction the potential is harmonic (coefficient of anharmonic fit is zero). The above displacement potential energy analysis confirms that the  $Pnmn$  phase is more anharmonic than  $I4/mmm$  phase. This is further confirmed by plotting the mean square displacements (MSD) for Bi and S atoms which are shown in Figure 7(c) for both  $Pnmn$  and  $I4/mmm$  phases. The MSD for Bi and S atoms are higher in  $Pnmn$  phase (Bi =  $0.012 \text{ \AA}^2$ , and S =  $0.024 \text{ \AA}^2$  at 300 K), than in the  $I4/mmm$  phase (Bi =  $0.009 \text{ \AA}^2$ , and S =  $0.011 \text{ \AA}^2$  at 300 K). This is expected because the longer Bi-S2 bond lengths in  $Pnmn$  phase make the atoms move easily from their equilibrium positions during the vibration than in the  $I4/mmm$  phase. Overall, the anharmonicity of the  $6s^2$  lone pair of  $Bi^{3+}$  cation plays a pivotal role in determining the phonon transport in  $Bi_2O_2S$  and it is suppressed (in  $I4/mmm$  phase) upon compression as can be seen from chemical pre-compression of Se/Te

atoms in  $Bi_2O_2Se$  and  $Bi_2O_2Te$ .<sup>19,20</sup>

## Conclusions

In summary, we have systematically investigated the effect of hydrostatic pressure on stereochemically active  $6s^2$  lone pair containing  $Bi_2O_2S$  with weak electrostatic interlayer bonding, and their implications on crystal structure, lattice dynamics and phonon transport properties using first principles calculations and Boltzmann transport theory. We predict that  $Bi_2O_2S$  undergoes a continuous structural phase transition from low symmetry distorted ( $Pnmn$ ) structure to a high symmetry ordered ( $I4/mmm$ ) structure at around 4 GPa, which is comparable to the transition pressure 6.4 GPa determined from the HP-XRD measurements.<sup>26</sup> The mechanical and dynamical stability of both  $Pnmn$  and  $I4/mmm$  phases are confirmed from the calculated elastic constants and phonon dispersion curves, respectively. The obtained enhanced Born effective charges (BECs) clearly demonstrate that both the phases show significant cross-band-gap hybridization from their electronic structure suggesting near ferroelectric instability and is favorable to achieve low  $\kappa_l$ . The obtained low average  $\kappa_l$  value 1.71 W-m/K for  $Pnmn$  phase over 4.93 W-m/K for  $I4/mmm$  phase is due to suppression of lone pair of  $Bi^{3+}$  cation at high pressure which reduces anharmonicity in  $I4/mmm$

phase. Both  $\kappa_l^{\parallel}$  and  $\kappa_l^{\perp}$  monotonically increase with applied pressure and become 14 W/m-K, and 10.5 W/m-K at 20 GPa, respectively. The highly anharmonic behavior of Bi and S atoms of *Pnmn* phase demonstrated from PES and MSD at ambient pressure is mainly responsible for low  $\kappa_l$ . Overall, the present work provides an insight on how hydrostatic pressure effects the chemical bonding, lattice dynamics and phonon transport in Bi<sub>2</sub>O<sub>2</sub>S. The present study could stimulate exploring pressure dependent phonon transport properties in materials especially with lone pair cation, which will provide a new avenue of pressure modulated low  $\kappa_l$  materials for future thermal energy applications.

## Acknowledgments

NYK and TP contributed equally to this manuscript. NYK would like to thank Institute for Advanced Computational Science, Stony Brook University for providing computational resources (Seawulf cluster). TP is supported by Research Foundation Flanders (FWO-VI). SCRR would like to thank RGUKT Basar for providing computational facilities.

## Supporting Information

Convergence tests of  $\kappa_l$  w.r.t cutoff distance and Gaussian broadening (Fig. S1), coherence contribution to  $\kappa_l$  (Fig. S2), Phonon life time and mean free paths (Fig. S3), pressure dependent variation of bond parameters (Figs. S4 and S5), centering of Bi<sup>3+</sup> cation with pressure (Fig. S6), pressure dependent variation of ICOHP (Fig. S7), Electronic and phonon band structures of *Pnmn* and *I4/mmm* phases at high pressure phases (Figs. S8 and S9), phonon group velocities at high pressure (Fig. S10) and pressure variation of thermal transport anisotropy (Fig. S11) (PDF).

## References

- (1) Zeier, W. G.; Zevalkink, A.; Gibbs, Z. M.; Hautier, G.; Kanatzidis, M. G.; Snyder, G. J. Thinking like a chemist: intuition in thermoelectric materials. *Angewandte Chemie International Edition* **2016**, *55*, 6826–6841.
- (2) Skoug, E. J.; Morelli, D. T. Role of lone-pair electrons in producing minimum thermal conductivity in nitrogen-group chalcogenide compounds. *Physical review letters* **2011**, *107*, 235901.
- (3) Tan, G.; Zhao, L.-D.; Kanatzidis, M. G. Rationally designing high-performance bulk thermoelectric materials. *Chemical reviews* **2016**, *116*, 12123–12149.
- (4) Du, B.; Zhang, R.; Chen, K.; Mahajan, A.; Reece, M. J. The impact of lone-pair electrons on the lattice thermal conductivity of the thermoelectric compound CuSbS<sub>2</sub>. *Journal of Materials Chemistry A* **2017**, *5*, 3249–3259.
- (5) Laurita, G.; Seshadri, R. Chemistry, Structure, and Function of Lone Pairs in Extended Solids. *Accounts of Chemical Research* **2022**, *55*, 1004–1014, PMID: 35319202.
- (6) Pal, K.; He, J.; Wolverton, C. Bonding Hierarchy Gives Rise to High Thermoelectric Performance in Layered Zintl Compound BaAu<sub>2</sub>P<sub>4</sub>. *Chemistry of Materials* **2018**, *30*, 7760–7768.
- (7) Pandey, T.; Nissimagoudar, A. S.; Mishra, A.; Singh, A. K. Ultralow thermal conductivity and high thermoelectric figure of merit in mixed valence In<sub>5</sub>X<sub>5</sub>Br (X= S, and Se) compounds. *Journal of Materials Chemistry A* **2020**, *8*, 13812–13819.
- (8) Yang, F.; Wang, R.; Zhao, W.; Jiang, J.; Wei, X.; Zheng, T.; Yang, Y.; Wang, X.; Lu, J.; Ni, Z. Thermal transport and energy dissipation in two-dimensional

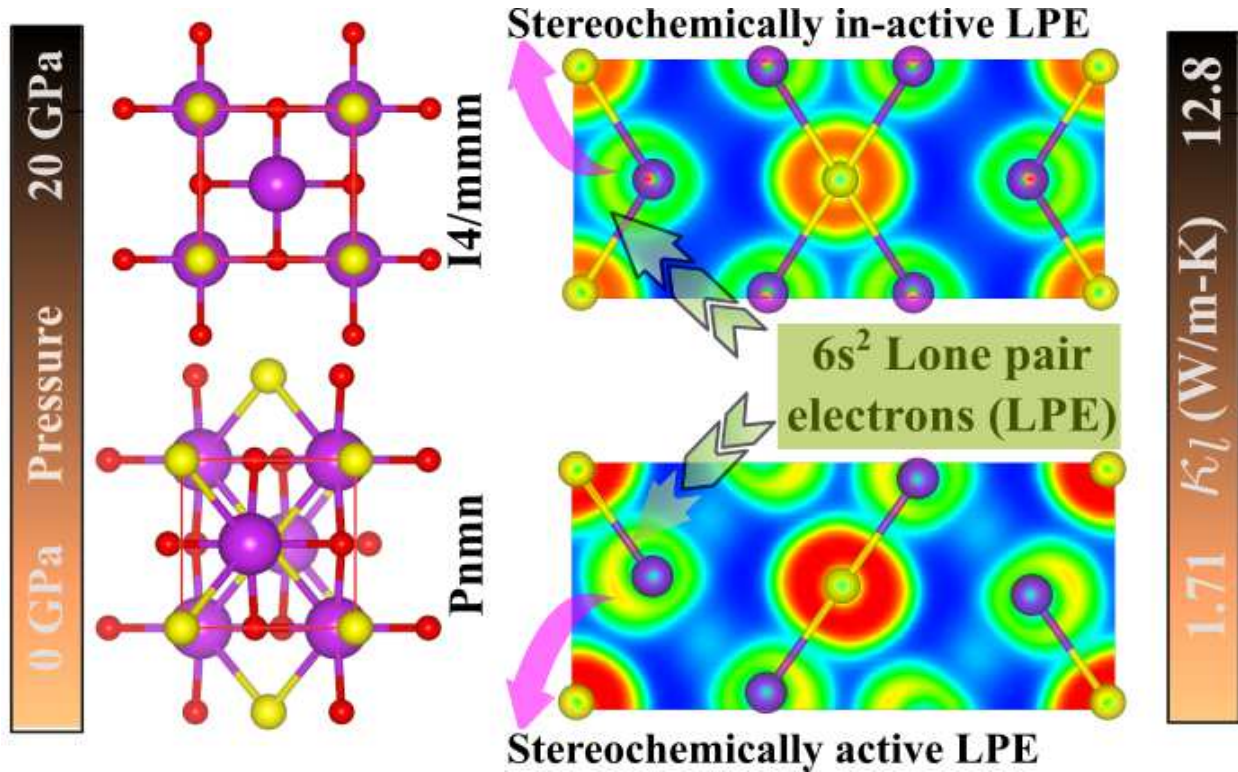
- Bi<sub>2</sub>O<sub>2</sub>Se. *Applied Physics Letters* **2019**, *115*, 193103.
- (9) Li, T.; Peng, H. 2D Bi<sub>2</sub>O<sub>2</sub>Se: An Emerging Material Platform for the Next-Generation Electronic Industry. *Accounts of Materials Research* **2021**, *2*, 842–853.
  - (10) Liang, Y.; Zhou, X.; Li, W.; Peng, H. Preparation of two-dimensional [Bi<sub>2</sub>O<sub>2</sub>]-based layered materials: Progress and prospects. *APL Materials* **2021**, *9*, 060905.
  - (11) Tippireddy, S.; D S, P. K.; Das, S.; Mallik, R. C. Oxychalcogenides as Thermoelectric Materials: An Overview. *ACS Applied Energy Materials* **2021**, *4*, 2022–2040.
  - (12) Guo, B.; Guo, Y.; Xu, L. First-principles insight into the interfacial properties of epitaxial Bi<sub>2</sub>O<sub>2</sub>X (X = S, Se, Te) on SrTiO<sub>3</sub> substrates. *Journal of Physics and Chemistry of Solids* **2022**, *163*, 110601.
  - (13) Luu, S. D.; Vaquero, P. Synthesis, characterisation and thermoelectric properties of the oxytelluride Bi<sub>2</sub>O<sub>2</sub>Te. *Journal of Solid State Chemistry* **2015**, *226*, 219–223.
  - (14) Wang, J.; Hu, W.; Lou, Z.; Xu, Z.; Yang, X.; Wang, T.; Lin, X. Thermoelectric properties of Bi<sub>2</sub>O<sub>2</sub>Se single crystals. *Applied Physics Letters* **2021**, *119*, 081901.
  - (15) Wu, M.; Zeng, X. C. Bismuth Oxychalcogenides: A New Class of Ferroelectric/Ferroelastic Materials with Ultra High Mobility. *Nano Letters* **2017**, *17*, 6309–6314.
  - (16) Yang, X.; Qu, L.; Gao, F.; Hu, Y.; Yu, H.; Wang, Y.; Cui, M.; Zhang, Y.; Fu, Z.; Huang, Y.; Feng, W.; Li, B.; Hu, P. High-Performance Broadband Photoelectrochemical Photodetectors Based on Ultrathin Bi<sub>2</sub>O<sub>2</sub>S Nanosheets. *ACS Applied Materials & Interfaces* **2022**, *14*, 7175–7183.
  - (17) Zhang, X.; Liu, Y.; Zhang, G.; Wang, Y.; Zhang, H.; Huang, F. Thermal Decomposition of Bismuth Oxysulfide from Photoelectric Bi<sub>2</sub>O<sub>2</sub>S to Superconducting Bi<sub>4</sub>O<sub>4</sub>S<sub>3</sub>. *ACS Applied Materials & Interfaces* **2015**, *7*, 4442–4448.
  - (18) Guo, H.; Xiao, J.; Qu, J.; Legut, D.; Zhang, Q. Odd–Even Layer Effect of Bismuth Oxychalcogenide Nanosurfaces: A First-Principles Study. *The Journal of Physical Chemistry C* **2019**, *123*, 24024–24030.
  - (19) Wei, Q.; Li, R.; Lin, C.; Han, A.; Nie, A.; Li, Y.; Li, L.-J.; Cheng, Y.; Huang, W. Quasi-Two-Dimensional Se-Terminated Bismuth Oxychalcogenide (Bi<sub>2</sub>O<sub>2</sub>Se). *ACS Nano* **2019**, *13*, 13439–13444.
  - (20) Guo, R.; Jiang, P.; Tu, T.; Lee, S.; Sun, B.; Peng, H.; Yang, R. Electrostatic interaction determines thermal conductivity anisotropy of Bi<sub>2</sub>O<sub>2</sub>Se. *Cell Reports Physical Science* **2021**, *2*, 100624.
  - (21) Meng, X.; Pandey, T.; Jeong, J.; Fu, S.; Yang, J.; Chen, K.; Singh, A.; He, F.; Xu, X.; Zhou, J., et al. Thermal conductivity enhancement in MoS<sub>2</sub> under extreme strain. *Physical Review Letters* **2019**, *122*, 155901.
  - (22) Yedukondalu, N.; Babu, K. R.; Bheemalingam, C.; Singh, D. J.; Vaitheeswaran, G.; Kanchana, V. Electronic structure, optical properties, and bonding in alkaline-earth halofluoride scintillators: BaClF, BaBrF, and BaIF. *Phys. Rev. B* **2011**, *83*, 165117.
  - (23) Yedukondalu, N.; Shafique, A.; Rakesh Roshan, S. C.; Barhoumi, M.; Muthaiah, R.; Ehm, L.; Parise, J. B.; Schwingenschlögl, U. Lattice Instability and Ultralow Lattice Thermal Conductivity of Layered PbIF. *ACS Applied Materials & Interfaces* **2022**, *14*, 40738–40748, PMID: 36053500.

- (24) Xu, Y.-D.; Wang, C.; Lv, Y.-Y.; Chen, Y. B.; Yao, S.-H.; Zhou, J. Infrared and Raman spectra of  $\text{Bi}_2\text{O}_2\text{X}$  and  $\text{Bi}_2\text{OX}_2$  ( $\text{X} = \text{S}, \text{Se}, \text{and Te}$ ) studied from first principles calculations. *RSC Advances* **2019**, *9*, 18042–18049.
- (25) Cheng, T.; Tan, C.; Zhang, S.; Tu, T.; Peng, H.; Liu, Z. Raman Spectra and Strain Effects in Bismuth Oxychalcogenides. *The Journal of Physical Chemistry C* **2018**, *122*, 19970–19980.
- (26) Bu, K.; Luo, H.; Guo, S.; Li, M.; Wang, D.; Dong, H.; Ding, Y.; Yang, W.; Lü, X. Pressure-Regulated Dynamic Stereochemical Role of Lone-Pair Electrons in Layered  $\text{Bi}_2\text{O}_2\text{S}$ . *The Journal of Physical Chemistry Letters* **2020**, *11*, 9702–9707.
- (27) Pereira, A. L. J. et al. Experimental and Theoretical Study of  $\text{Bi}_2\text{O}_2\text{Se}$  Under Compression. *The Journal of Physical Chemistry C* **2018**, *122*, 8853–8867.
- (28) Wang, Y. X.; Yan, Z. X.; Liu, W.; Zhou, G. L.; Gu, J. B. Ab initio study of the mechanical properties and thermal conductivity of  $\text{Bi}_2\text{O}_2\text{X}$  ( $\text{X} = \text{Se}, \text{Te}$ ) under pressure. *Solid State Sciences* **2020**, *106*, 106299.
- (29) Wang, C.; Ding, G.; Wu, X.; Wei, S.; Gao, G. Electron and phonon transport properties of layered  $\text{Bi}_2\text{O}_2\text{Se}$  and  $\text{Bi}_2\text{O}_2\text{Te}$  from first-principles calculations. *New Journal of Physics* **2018**, *20*, 123014.
- (30) Song, H.-Y.; Ge, X.-J.; Shang, M.-Y.; Zhang, J.; Lü, J.-T. Intrinsically low thermal conductivity of bismuth oxychalcogenides originating from interlayer coupling. *Phys. Chem. Chem. Phys.* **2019**, *21*, 18259–18264.
- (31) Song, H.-Y.; Ge, X.-J.; Lü, J.-T. First-principles study on the electron and phonon transport properties of layered  $\text{Bi}_2\text{OX}_2$  ( $\text{X} = \text{S}, \text{Se}$ ). *AIP Advances* **2020**, *10*, 125314.
- (32) Ma, X.; Chang, D.; Zhao, C.; Li, R.; Huang, X.; Zeng, Z.; Huang, X.; Jia, Y. Geometric structures and electronic properties of the  $\text{Bi}_2\text{X}_2\text{Y}$  ( $\text{X}, \text{Y} = \text{O}, \text{S}, \text{Se}, \text{and Te}$ ) ternary compound family: a systematic DFT study. *Journal of Materials Chemistry C* **2018**, *6*, 13241–13249.
- (33) Hu, C.-W.; Yang, Y.; Hou, C.; Liang, T.-X. Chemical trends of structural, mechanical, electronic and optical properties of  $\text{Bi}_2\text{O}_2\text{X}$  ( $\text{X} = \text{S}, \text{Se}, \text{Te}$ ): A first-principles study. *Materials Today Communications* **2020**, *25*, 101619.
- (34) Kresse, G.; Furthmüller, J. Efficient iterative schemes for ab initio total-energy calculations using a plane-wave basis set. *Physical Review B* **1996**, *54*, 11169–11186.
- (35) Grimme, S.; Ehrlich, S.; Goerigk, L. Effect of the damping function in dispersion corrected density functional theory. *Journal of Computational Chemistry* **2011**, *32*, 1456–1465.
- (36) Tran, F.; Blaha, P. Accurate Band Gaps of Semiconductors and Insulators with a Semilocal Exchange-Correlation Potential. *Physical Review Letters* **2009**, *102*.
- (37) Momma, K.; Izumi, F. VESTA: a three-dimensional visualization system for electronic and structural analysis. *Journal of Applied Crystallography* **2008**, *41*, 653–658.
- (38) Nelson, R.; Ertural, C.; George, J.; Deringer, V. L.; Hautier, G.; Dronskowski, R. LOBSTER: Local orbital projections, atomic charges, and chemical-bonding analysis from projector-augmented-wave-based density-functional theory. *Journal of Computational Chemistry* **2020**, *41*, 1931–1940.
- (39) Togo, A.; Tanaka, I. First principles phonon calculations in materials science. *Scripta Materialia* **2015**, *108*, 1–5.



- (40) Wang, Y.; Wang, J.; Wang, W.; Mei, Z.; Shang, S.; Chen, L.; Liu, Z. A mixed-space approach to first-principles calculations of phonon frequencies for polar materials. *Journal of Physics: Condensed Matter* **2010**, *22*, 202201.
- (41) Li, W.; Mingo, N.; Lindsay, L.; Broido, D. A.; Stewart, D. A.; Katcho, N. A. Thermal conductivity of diamond nanowires from first principles. *Physical Review B* **2012**, *85*, 195436.
- (42) Li, W.; Lindsay, L.; Broido, D. A.; Stewart, D. A.; Mingo, N. Thermal conductivity of bulk and nanowire  $\text{Mg}_2\text{Si}_x\text{Sn}_{1-x}$  alloys from first principles. *Physical Review B* **2012**, *86*, 174307.
- (43) Li, W.; Carrete, J.; Katcho, N. A.; Mingo, N. ShengBTE: A solver of the Boltzmann transport equation for phonons. *Computer Physics Communications* **2014**, *185*, 1747–1758.
- (44) Tamura, S.-i. Isotope scattering of dispersive phonons in Ge. *Physical Review B* **1983**, *27*, 858.
- (45) Simoncelli, M.; Marzari, N.; Mauri, F. Unified theory of thermal transport in crystals and glasses. *Nature Physics* **2019**, *15*, 809–813.
- (46) Luo, Y.; Yang, X.; Feng, T.; Wang, J.; Ruan, X. Vibrational hierarchy leads to dual-phonon transport in low thermal conductivity crystals. *Nature Communications* **2020**, *11*, 1–10.
- (47) Xia, Y.; Ozoliņš, V.; Wolverton, C. Microscopic mechanisms of glasslike lattice thermal transport in cubic  $\text{Cu}_{12}\text{Sb}_4\text{S}_{13}$  tetrahedrites. *Physical Review Letters* **2020**, *125*, 085901.
- (48) Jain, A. Multichannel thermal transport in crystalline  $\text{Tl}_3\text{VSe}_4$ . *Physical Review B* **2020**, *102*, 201201.
- (49) Pandey, T.; Du, M.-H.; Parker, D. S.; Lindsay, L. Origin of ultralow phonon transport and strong anharmonicity in lead-free halide perovskites. *Materials Today Physics* **2022**, 100881.
- (50) Hardy, R. J. Energy-flux operator for a lattice. *Physical Review* **1963**, *132*, 168.
- (51) Allen, P. B.; Feldman, J. L. Thermal conductivity of disordered harmonic solids. *Physical Review B* **1993**, *48*, 12581.
- (52) Becke, A. D.; Edgecombe, K. E. A simple measure of electron localization in atomic and molecular systems. *The Journal of chemical physics* **1990**, *92*, 5397–5403.
- (53) Seshadri, R.; Hill, N. A. Visualizing the role of Bi 6s “lone pairs” in the off-center distortion in ferromagnetic  $\text{BiMnO}_3$ . *Chemistry of materials* **2001**, *13*, 2892–2899.
- (54) Klotz, S.; Chervin, J.-C.; Munsch, P.; Marchand, G. L. Hydrostatic limits of 11 pressure transmitting media. *Journal of Physics D: Applied Physics* **2009**, *42*, 075413.
- (55) Heyd, J.; Peralta, J. E.; Scuseria, G. E.; Martin, R. L. Energy band gaps and lattice parameters evaluated with the Heyd-Scuseria-Ernzerhof screened hybrid functional. *The Journal of Chemical Physics* **2005**, *123*, 174101.
- (56) Verma, P.; Truhlar, D. G. HLE16: A Local Kohn–Sham Gradient Approximation with Good Performance for Semiconductor Band Gaps and Molecular Excitation Energies. *The Journal of Physical Chemistry Letters* **2017**, *8*, 380–387.
- (57) Shi, H.; Ming, W.; Du, M.-H. Bismuth chalcogenides and oxyhalides as optoelectronic materials. *Phys. Rev. B* **2016**, *93*, 104108.
- (58) Du, M.-H.; Singh, D. J. Enhanced Born charge and proximity to ferroelectricity in thallium halides. *Phys. Rev. B* **2010**, *81*, 144114.

- (59) Du, M.-H.; Singh, D. J. Enhanced Born charges in III-VII, IV-VII<sub>2</sub>, and V-VII<sub>3</sub> compounds. *Phys. Rev. B* **2010**, *82*, 045203.
- (60) Pandey, T.; Lindsay, L.; Sales, B. C.; Parker, D. S. Lattice instabilities and phonon thermal transport in TlBr. *Physical Review Materials* **2020**, *4*, 045403.
- (61) Mouhat, F.; Coudert, F.-X. Necessary and sufficient elastic stability conditions in various crystal systems. *Physical Review B* **2014**, *90*.
- (62) Sinko, G. V.; Smirnov, N. A. Ab initio calculations of elastic constants and thermodynamic properties of bcc, fcc, and hcp Al crystals under pressure. *Journal of Physics: Condensed Matter* **2002**, *14*, 6989–7005.
- (63) Sinko, G. V.; Smirnov, N. A. On elasticity under pressure. *Journal of Physics: Condensed Matter* **2004**, *16*, 8101–8104.
- (64) Yedukondalu, N.; Vaitheeswaran, G.; Anees, P.; Valsakumar, M. C. Phase stability and lattice dynamics of ammonium azide under hydrostatic compression. *Phys. Chem. Chem. Phys.* **2015**, *17*, 29210–29225.
- (65) Nielsen, M. D.; Ozolins, V.; Heremans, J. P. Lone pair electrons minimize lattice thermal conductivity. *Energy & Environmental Science* **2013**, *6*, 570–578.
- (66) Zhang, R.; Zhou, Z.; Qi, N.; Zhao, B.; Zhang, Q.; Zhang, Z.; Chen, Z. Significant enhancement in the thermoelectric performance of Bi<sub>2</sub>O<sub>2</sub>S through dimensionality reduction. *Journal of Materials Chemistry C* **2019**, *7*, 14986–14992.
- (67) Witting, I. T.; Chasapis, T. C.; Ricci, F.; Peters, M.; Heinz, N. A.; Hautier, G.; Snyder, G. J. The thermoelectric properties of bismuth telluride. *Advanced Electronic Materials* **2019**, *5*, 1800904.
- (68) Paulatto, L.; Fournier, D.; Marangolo, M.; Eddrief, M.; Atkinson, P.; Calandra, M. Thermal conductivity of Bi<sub>2</sub>Se<sub>3</sub> from bulk to thin films: Theory and experiment. *Physical Review B* **2020**, *101*, 205419.
- (69) Biswas, K.; Zhao, L.-D.; Kanatzidis, M. G. Tellurium-Free Thermoelectric: The Anisotropic n-Type Semiconductor Bi<sub>2</sub>S<sub>3</sub>. *Advanced Energy Materials* **2012**, *2*, 634–638.
- (70) Pandey, T.; Singh, A. K. Simultaneous enhancement of electrical conductivity and thermopower in Bi<sub>2</sub>S<sub>3</sub> under hydrostatic pressure. *Journal of Materials Chemistry C* **2016**, *4*, 1979–1987.



Effect of hydrostatic pressure on stereochemically active  $6s^2$  lone pair of  $\text{Bi}^{3+}$  cation in  $\text{Bi}_2\text{O}_2\text{S}$  (*Pnmm*) is systematically investigated.  $\text{Bi}_2\text{O}_2\text{S}$  transformed to  $\text{Bi}_2\text{O}_2\text{Se/Te}$ -type (*I4/mmm*) structure due to dynamic centering of  $\text{Bi}^{3+}$  cation. The active and in-active nature of lone pair has profound implications on phonon transport, which aid for in silico design of advanced energy conversion materials.

# Supporting Information

## Effect of Hydrostatic Pressure on Lone Pair Activity and Phonon Transport in $\text{Bi}_2\text{O}_2\text{S}$

Neelam Yedukondalu,<sup>\*,†,‡,¶</sup> Tribhuwan Pandey,<sup>\*,§</sup> and S Chand Rakesh

Roshan<sup>||,⊥</sup>

<sup>†</sup>*Department of Analytical and Structural Chemistry, CSIR-Indian Institute of Chemical Technology, Tarnaka, Hyderabad 500007, India*

<sup>‡</sup>*Department of Geosciences, Center for Materials by Design, and Institute for Advanced Computational Science, State University of New York, Stony Brook, New York 11794-2100, USA*

<sup>¶</sup>*Joint Photon Sciences Institute, Stony Brook University, Stony Brook, New York 11790-2100, USA*

<sup>§</sup>*Department of Physics, University of Antwerp, Groenenborgerlaan 171, B-2020 Antwerp, Belgium*

<sup>||</sup>*Rajiv Gandhi University of Knowledge Technologies, Basar, Telangana-504107, India*

<sup>⊥</sup>*Department of Physics, National Institute of Technology-Warangal, Telangana, India*

E-mail: nykondalu@gmail.com; tribhuwan.pandey@uantwerpen.be

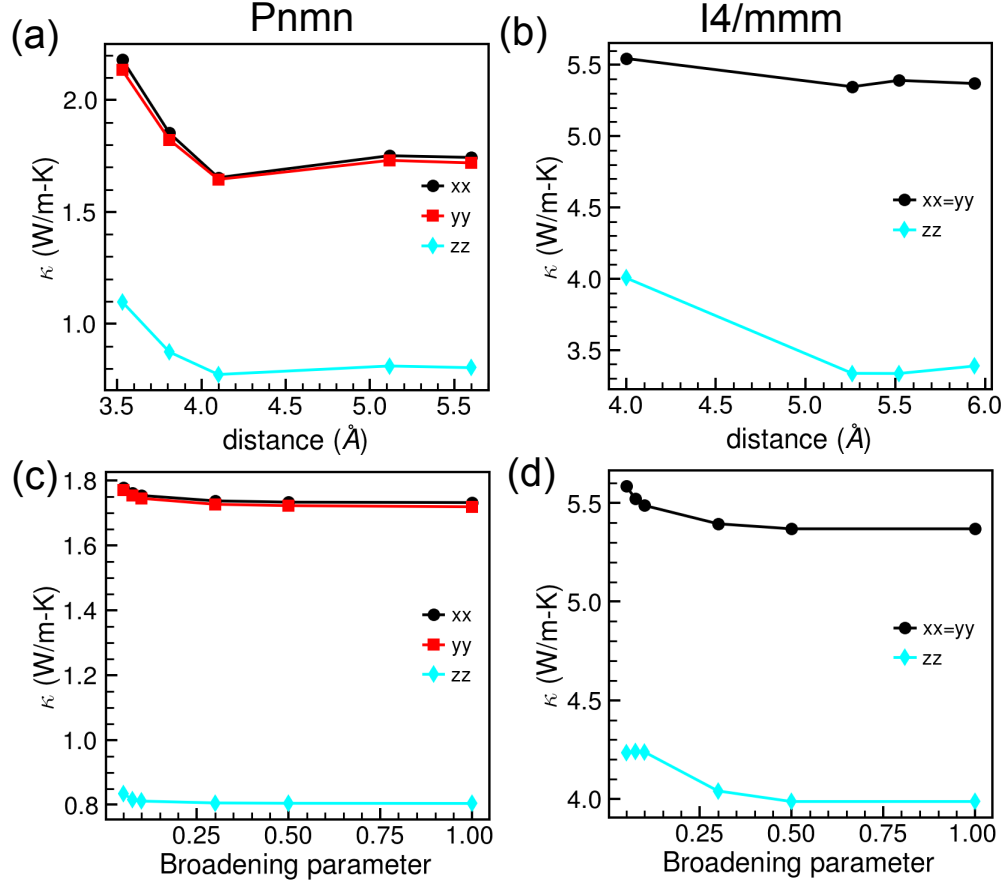


Figure S1: Convergence of calculated lattice thermal conductivity (without coherence term) with respect to cutoff distance for 3<sup>rd</sup> order interatomic force constants for (a) 0 GPa *Pnmn* (b) 5 GPa *I4/mmm* phases of Bi<sub>2</sub>O<sub>2</sub>S. Convergence of calculated lattice thermal conductivity with respect to Gaussian broadening parameters at (a) 0 GPa for *Pnmn* phase (b) 5 GPa *I4/mmm* phases of Bi<sub>2</sub>O<sub>2</sub>S. These calculations are performed at k-mesh of 21×21×7, and for panel (a) and (b) broadening parameter of 1.0 was used.

## Coherence thermal conductivity

At 0 GPa, room temperature  $\kappa_c$  value is  $\sim 0.3$  W/m-K, and the same is reduced to 0.17 W/m-K at 20 GPa. The calculated  $\kappa_c$  contributions can be understood by analysis of phonon mean free path ( $\Lambda$ ) and phonon lifetimes ( $\tau$ ) as a function of phonon frequency which are shown in Figure S3. Within the Ioffe Regal limit, phonons are characterized as well-defined in space (time) when mean free paths are greater than the average atomic spacing  $a$  ( $\Lambda > a$ ) (lifetimes are greater than the reciprocal angular frequency  $\tau > 1/\omega$ ).<sup>1-3</sup> These phonons

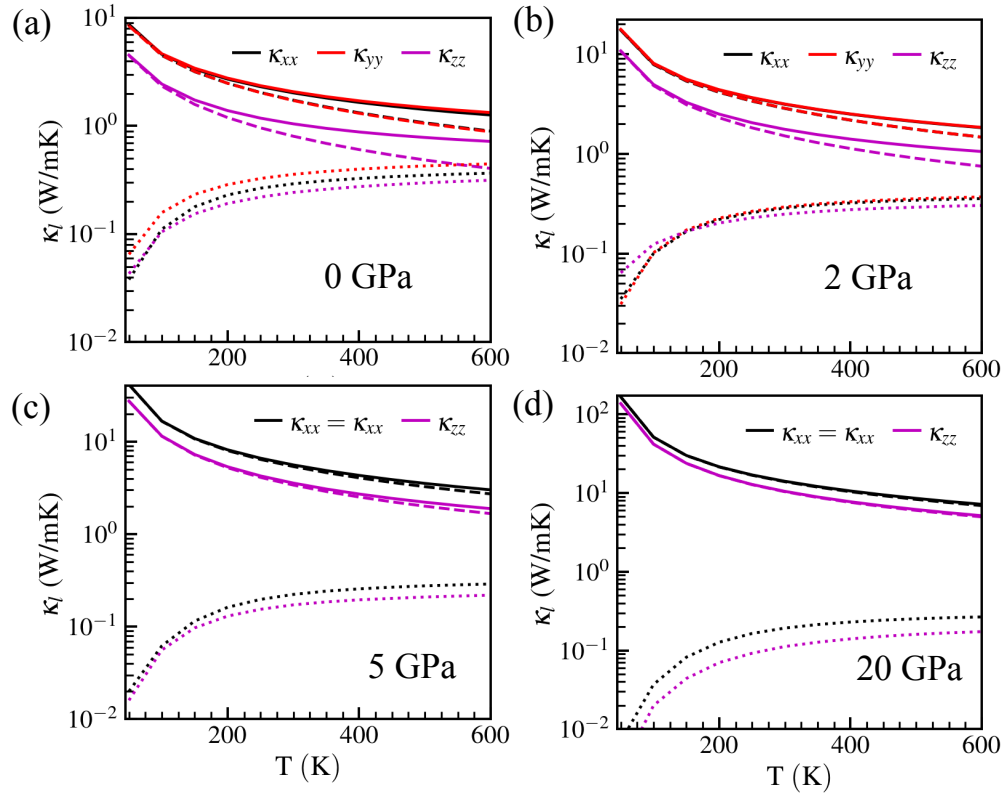


Figure S2: Calculated temperature dependent thermal conductivities of  $\text{Bi}_2\text{O}_2\text{S}$  at (a) 0 GPa, (b) 2 GPa, (c) 5 GPa and (d) 20 GPa pressures. Here dashed, and dotted lines represent thermal conductivity due to particle ( $\kappa_p$ ) and coherence ( $\kappa_c$ ) channels, respectively. Summation of  $\kappa_l$  and  $\kappa_c$  gives total lattice thermal conductivity from both channels.

mainly contribute to particle like thermal conduction ( $\kappa_p$ ). Whereas phonons with  $\Lambda < a$  and  $\tau < 1/\omega$  contribute to coherence conductivity ( $\kappa_c$ ). As shown below is Figure S3 (a), at all pressure values phonon are well-defined in time ( $\tau > 1/\omega$ ) and only few phonons modes satisfy  $\Lambda < a$  (Figure S3 (b)). When the pressure is applied  $\Lambda$  further increases and even fewer modes satisfy  $\Lambda < a$ . Therefore,  $\kappa_c$  contribution decreases with applied pressure.

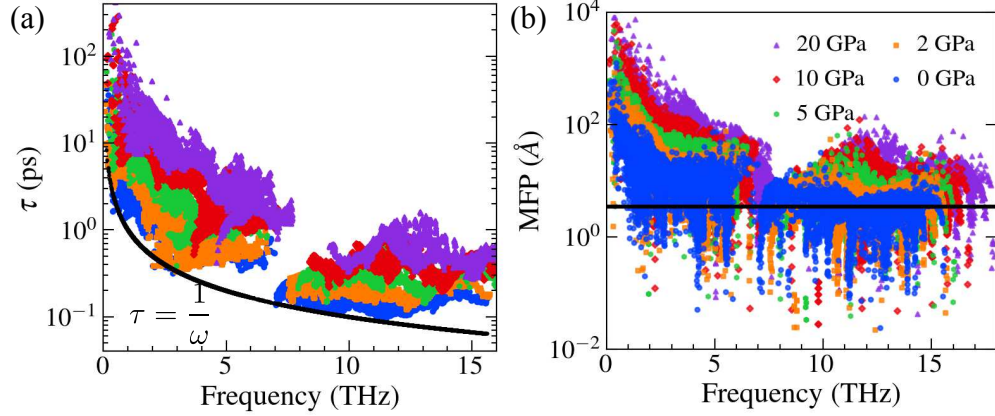


Figure S3: Room temperature (a) phonon lifetime ( $\tau$ ) and (b) phonon mean free paths ( $\Lambda$ ) as a function of phonon frequency. Black curve in (a) give the phonon lifetimes in the Ioffe Regel limit ( $\tau = 1/\omega$ ). Black horizontal line is the average bond length “a”.

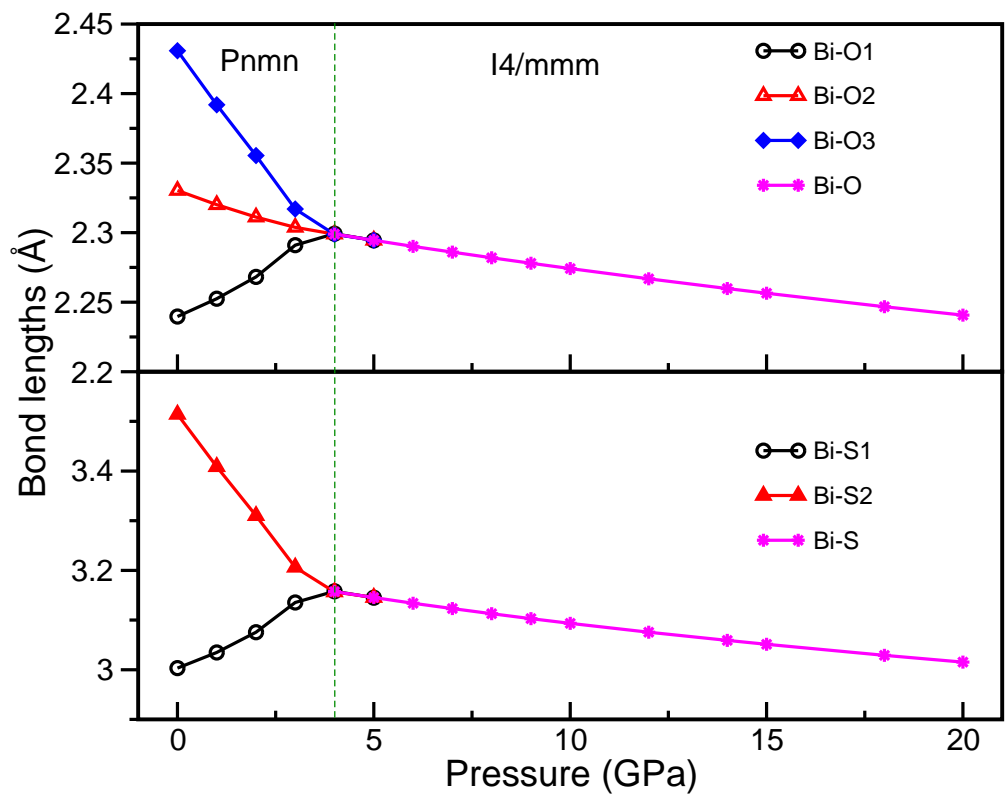


Figure S4: Calculated in-equivalent bond lengths of ambient ( $Pn\bar{m}n$ ) and high pressure ( $I4/m\bar{m}m$ ) phases of  $\text{Bi}_2\text{O}_2\text{S}$  as a function of pressure.



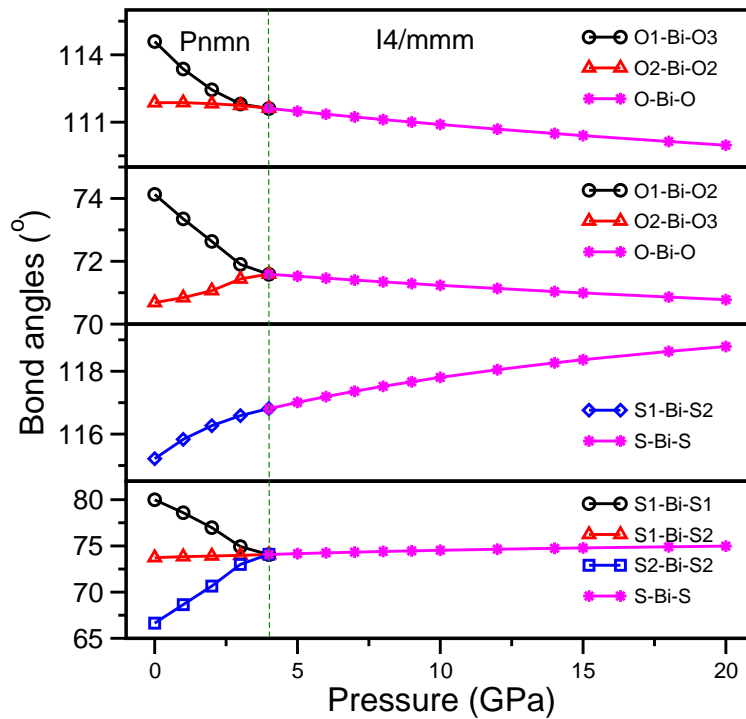


Figure S5: Calculated in-equivalent bond angles of ambient ( $Pnmm$ ) and high pressure ( $I4/mmm$ ) phases of  $\text{Bi}_2\text{O}_2\text{S}$  as a function of pressure.

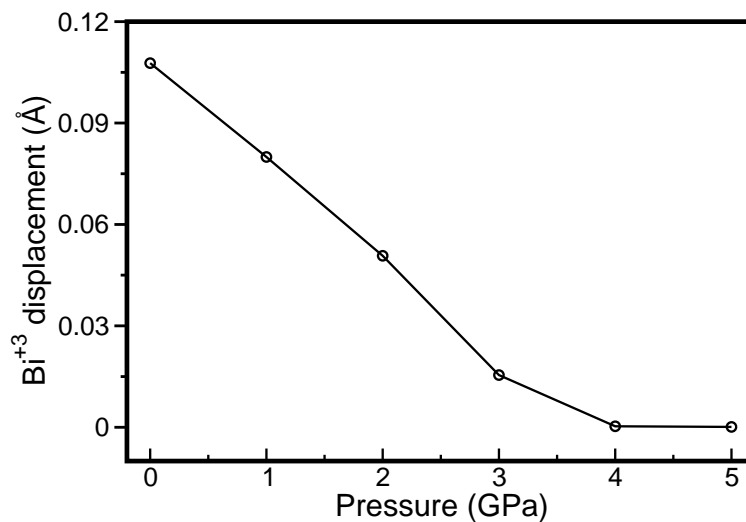


Figure S6: Centering of  $\text{Bi}^{3+}$  cation in ambient ( $Pnmm$ ) phase of  $\text{Bi}_2\text{O}_2\text{S}$  as a function of pressure.

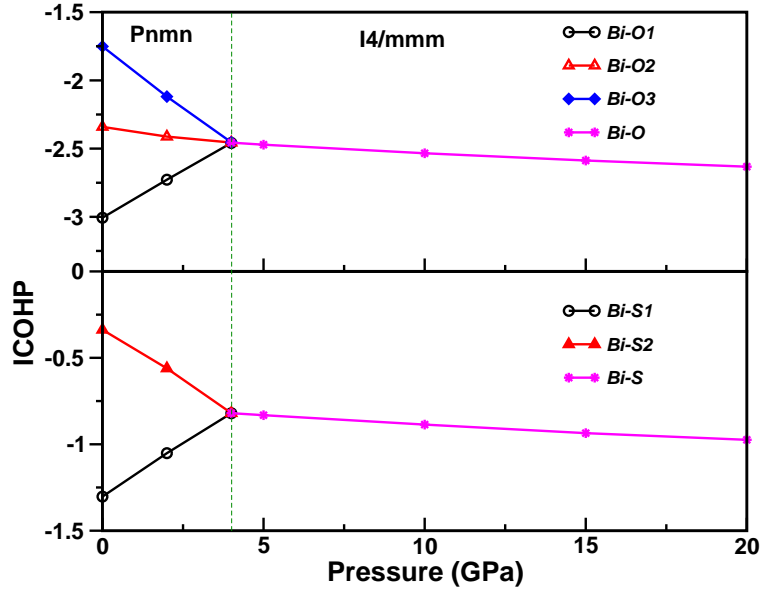


Figure S7: Calculated ICOHP values for in-equivalent bond lengths of ambient ( $Pnmm$ ) and high pressure ( $I4/mmm$ ) phases of  $\text{Bi}_2\text{O}_2\text{S}$  as a function of pressure.

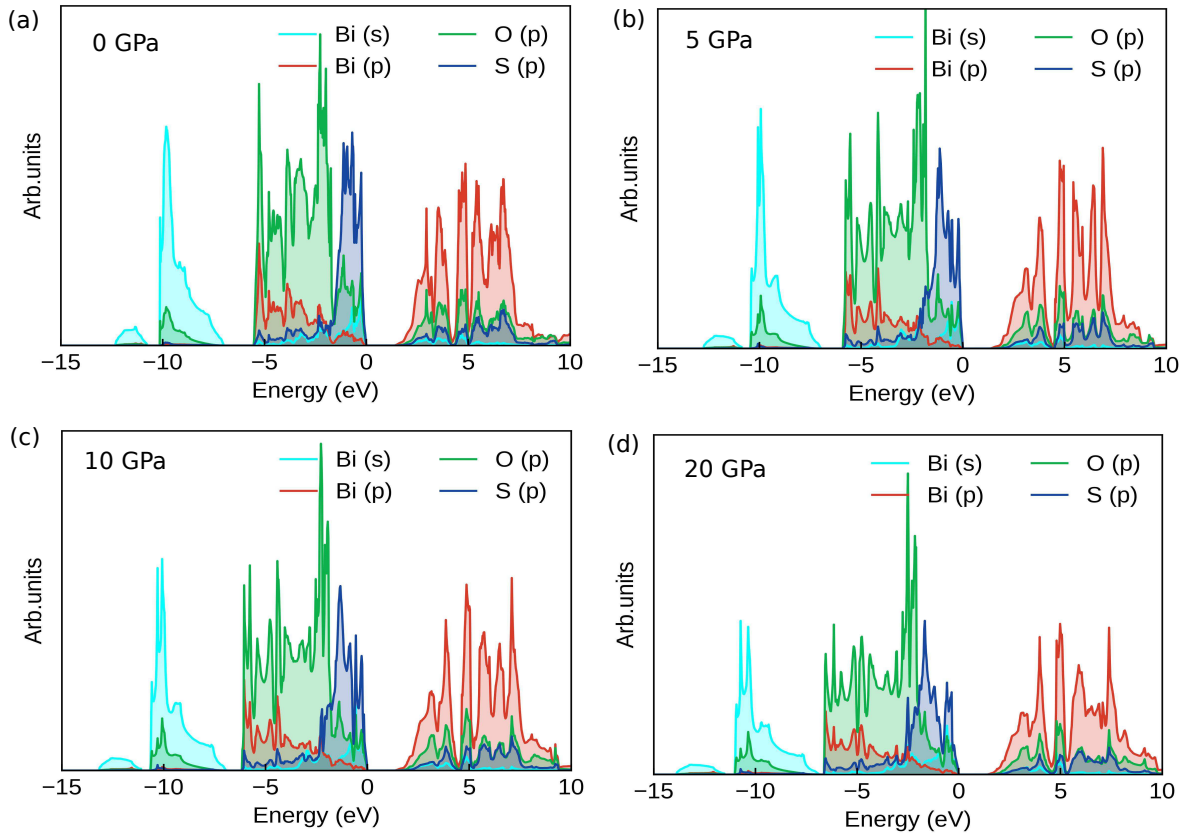


Figure S8: Calculated projected density of states at 0 GPa for ambient ( $Pnmm$ ) phase and at 5 GPa, 10 GPa and 20 GPa for high pressure ( $I4/mmm$ ) phase of  $\text{Bi}_2\text{O}_2\text{S}$ .

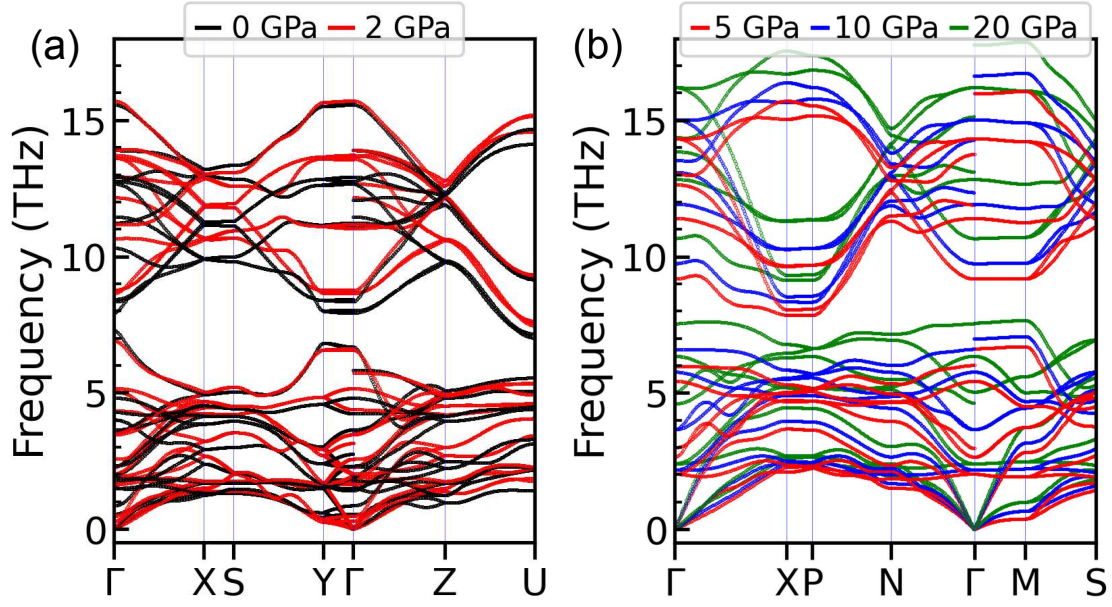


Figure S9: Calculated pressure dependent phonon dispersion curves of  $\text{Bi}_2\text{O}_2\text{S}$  in (a)  $Pnmm$  (0, and 2 GPa), and (b)  $I4/mmm$  (5, 10, and 20 GPa) phase.

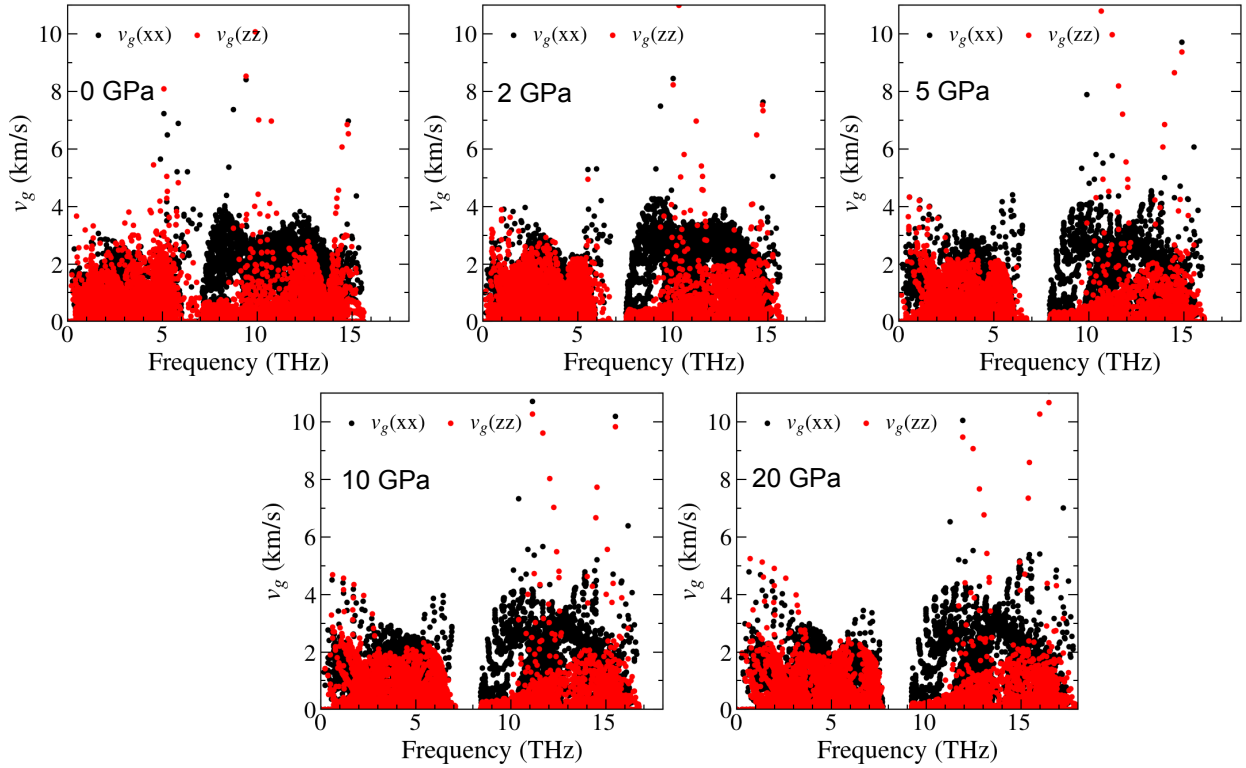


Figure S10: In plane (xx) and cross plane (zz) components of phonon group velocities as a function of frequencies at indicated pressures.

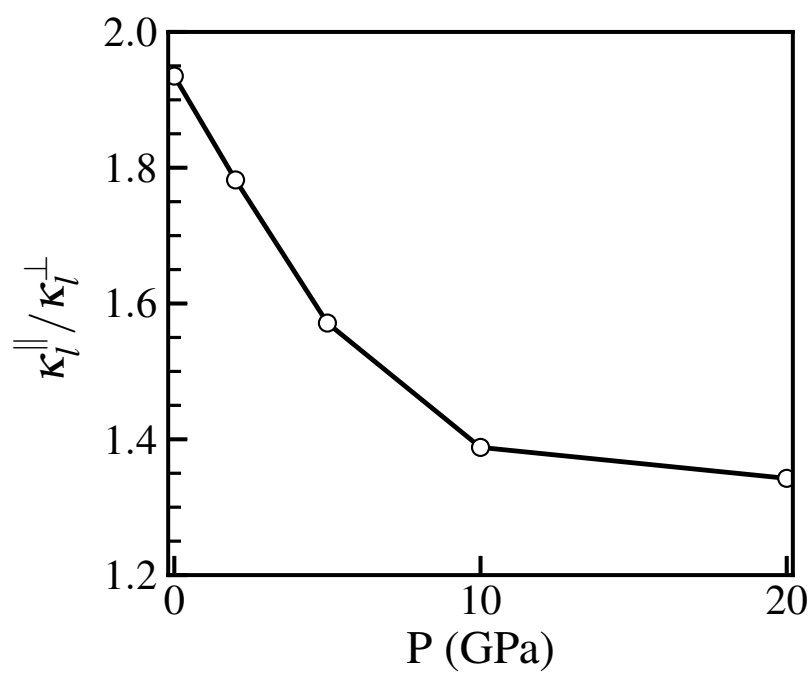


Figure S11: Effect of pressure on room temperature thermal transport anisotropy ( $\kappa_l^{\parallel} / \kappa_l^{\perp}$ ) as a function of pressure.

**Table S1: Bond parameters such as bond lengths (in Å) and bond angles (in °) of ambient ( $Pn\bar{m}n$ ) and high pressure ( $I4/m\bar{m}m$ ) phases of  $\text{Bi}_2\text{O}_2\text{S}$  obtained using DFT-D3 method.**

Phase (Pressure)	Parameter	This work	Others <sup>a</sup>
$Pn\bar{m}n$ (0 GPa)	Bi-S1	3.00	3.149
	Bi-S2	3.51	3.227
	Bi-O1	2.24	2.288
	Bi-O2	2.33	2.302
	Bi-O3	2.43	2.316
	$\angle$ S1-Bi-S1	80.00	
	$\angle$ S2-Bi-S2	66.64	
	$\angle$ S1-Bi-S2 ( $\times 2$ )	73.73	
		115.22	
	$\angle$ O1-Bi-O2	74.13	
	$\angle$ O2-Bi-O3	70.69	
	$\angle$ O2-Bi-O2	111.87	
	$\angle$ O1-Bi-O3	114.59	
	$I4/m\bar{m}m$ (5.6 GPa)	Bi-S	3.14
Bi-O		2.29	
$\angle$ S-Bi-S ( $\times 2$ )		74.21	
		117.12	
$\angle$ O-Bi-O ( $\times 2$ )		71.49	
		111.41	

<sup>a</sup>Ref. <sup>4</sup>

## References

- (1) Simoncelli, M.; Marzari, N.; Mauri, F. Unified theory of thermal transport in crystals and glasses. *Nature Physics* **2019**, *15*, 809–813.
- (2) Luo, Y.; Yang, X.; Feng, T.; Wang, J.; Ruan, X. Vibrational hierarchy leads to dual-phonon transport in low thermal conductivity crystals. *Nature Communications* **2020**, *11*, 1–10.
- (3) Pandey, T.; Du, M.-H.; Parker, D. S.; Lindsay, L. Origin of ultralow phonon transport and strong anharmonicity in lead-free halide perovskites. *Materials Today Physics* **2022**, 100881.
- (4) Hu, C.-W.; Yang, Y.; Hou, C.; Liang, T.-X. Chemical trends of structural, mechanical, electronic and optical properties of  $\text{Bi}_2\text{O}_2\text{X}$  ( $X = \text{S}, \text{Se}, \text{Te}$ ): A first-principles study. *Materials Today Communications* **2020**, *25*, 101619